APPENDIX C

NUMERICAL MODELLING OF SEISMIC-GENERATED WAVES

Prepared By:

Ocean Networks Canada

oceannetworks.ca

OCEAN NETWORKS CANADA

CO-SEISMIC TSUNAMI HAZARD ASSESSMENT FOR PRINCE RUPERT

AN INITIATIVE OF University of Victoria

CONTENTS

CO-SEISMIC TSUNAMI HAZARD ASSESSMENT FOR PRINCE RUPERT

Jeffrey C. Harris, LHSV, Ecole des Ponts, CEREMA, EDF R&D, Chatou, France
Reza Amouzgar, Ocean Networks Canada, University of Victoria, Victoria, British Columbia, Canada
Nathan Grivault, Ocean Networks Canada, University of Victoria, Victoria, British Columbia, Canada

ABSTRACT

The most significant co-seismic tsunami hazards of the western coast of Canada can be associated with either the Alaska-Aleutian subduction zone or the Cascadia subduction zone. For a small coastal town like Prince Rupert, being in the lee of many islands, such as Haida Gwaii, as well as many other smaller islands, one might assume that the tsunami risk is minimal, but it is known that occasionally tsunamis are magnified behind islands, such as in the 1992 Flores tsunami off Indonesia. In this work, the nonlinear Boussinesq model FUNWAVE-TVD is used for studying the wave propagation and inundation, both an Alaska-Aleutian subduction zone event and a Cascadia subduction zone event, under present conditions, as well as under a 1.0 m sea-level rise corresponding to expected climate change in the next century. Simulations indicate that while the Cascadia subduction event could be devastating elsewhere, another earthquake off the Alaska coast such as the 1964 event would affect Prince Rupert more strongly. Additionally, as these calculations did not consider an exhaustive look at possible events, a safety factor should be added to the impacts of such an event.

1. INTRODUCTION

Subduction zones around the Pacific margin have caused many large earthquakes and represent a significant tsunami hazard to western Canada. This includes the extremely active Alaska-Aleutian subduction zone as well as the Cascadia subduction zone; more distant sources of tsunamis may be more frequent, but pose a smaller risk to the city of Prince Rupert (Dunbar et al., 1988). Although there have been numerous studies of tsunami risks in the area, including Prince Rupert (e.g., Fine et al., 2018a, 2018b), the understanding of the potential sources and the numerical models available have improved substantially in recent years.

Most recently, on 23 January 2018, there was a M_w 7.9 earthquake off Alaska, without any tsunami alert in the coastal city of Prince Rupert. Local warning systems in British Columbia vary dramatically; for example, tsunami warnings may be sent by the Prince Rupert Marine Communications and Traffic Services Division (Anderson and Gow, 2004). Prior to this event, there had been seven co-seismic tsunamis with records at Prince Rupert, including the 1964 Alaska tsunami which caused a 1.4 meter wave (above the tidal level) at the city, with an observed period around 92 minutes (Wigen and White, 1964).

Although in some cases one might expect that islands offshore such as Haida Gwaii or Digby Island would provide protection to a coastal city from incoming waves, in fact, tsunami hazard can be

higher in the lee side of islands (Stefanakis et al., 2014). The focusing effect on the lee side of islands became particularly evident after the 1992 Flores tsunami in Indonesia (Liang et al., 2011).

In this report, we consider the effect of a number of different scenarios which could pose a realistic threat to the city, as well as expected sea-level rise over the next century for future hazard prediction.

2. CO-SEISMIC HAZARDS

There are a number of approaches possible to assess tsunami hazard, both deterministic (e.g., Wronna et al., 2015) and probabilistic (e.g., Geist and Parsons, 2006). In this project, we make use of a deterministic approach, selecting the most significant credible tsunami scenarios for the study area.

2.1 Alaska-Aleutian subduction zone

The Alaska-Aleutian subduction zone is the origin of numerous significant earthquakes of magnitude 8 and more (e.g., M_w 8.3 in 1938, 1946 M_w 8.6, 1957 M_w 8.6, 1964 M_w 9.2, 1965 M_w 8.7; see Dunbar and Weaver, 2008), and further back has been active for some time (Nelson et al., 2015). The largest of the recent earthquakes, namely, the 1964 Alaska earthquake produced the largest instrumentally-recorded tsunami waves to date on the British Columbia coast (Wigen and White, 1964), and this event represents a realistic proxy for similar large events generated by the subduction zone. This scenario will be examined in this study.

A number of different inversions of the event have been created; here we consider three representative ones (Johnson et al., 1996; Suito and Freymueller, 2009; Ichinose et al., 2007); in order to best understand the risk from this subduction zone, each source will be considered below. Johnson et al. (1996), for example, used a joint inversion of tsunami waveforms and geodetic data to determine a set of subfaults for the detailed slip distribution more accurately than earlier tests (e.g., Christensen and Beck, 1994).

The resulting tsunami on the BC coast from such an earthquake has been also studied previously; Fine et al. (2018a) found that tsunami-induced currents in Fern Passage (near Prince Rupert) could be as high as 2.5 m/s. They also were able to reproduce the waveform observed at the tidal gauge in the Prince Rupert Harbour.

2.2 Cascadia subduction zone

Great megathrust earthquakes occur on the Cascadia subduction zone roughly once every 500 years (Goldfinger et al., 2012). The last great Cascadia earthquake was in 1700, and while there is no written record of the impact along the eastern Pacific, it was recorded in oral history (e.g., Ludwin et al., 2005) and in the coastal and offshore stratigraphy at sites from northern California to Vancouver Island (e.g., Atwater et al., 1995; Goldfinger et al. 2012).

For characteristic scenarios, we make use of the source models developed by Gao et al. (2018). From the four different variants that have been developed, low-resolution tsunami simulation indicates

that a splay faulting rupture can generate 50-100% higher wave surface elevation compared to buried rupture (Gao et al., 2018). This suggests that this scenario has the greatest potential impact on the west coast and Prince Rupert and thus will be explored in this study.

A similar scenario has been modelled by Fine et al. (2018b), who found that tsunami-induced currents in nearby Fern Passage could be as high as 2 m/s. They also predicted the highest wave height can reach to 0.76 m at Seal Cove above the tidal range in Prince Rupert Harbour area.

2.3 Co-seismic tsunami hazard from faults in the Haida Gwaii and Hecate strait regions

Another possible source of tsunamis is the Haida Gwaii margin, which hosts the boundary between the Pacific and North America plates. This plate boundary is seismically active and is located about 250 km west of Prince Rupert, trending northwest from offshore southern Haida Gwaii toward southeastern Alaska. North of the Haida Gwaii islands, relative plate motion is approximately parallel to the plate boundary, and earthquakes are dominated by strike-slip mechanisms on the near-vertical Queen Charlotte fault; in these events, co-seismic seafloor motion is near-horizontal, so they do not typically generate significant tsunamis. The Queen Charlotte fault was the source of Canada's largest instrumentally-recorded earthquake, the Mw 8.1 Queen Charlotte earthquake in 1949 (e.g., Cassidy et al., 2010). Although, as expected, seafloor displacements did not directly generate a significant tsunami, the earthquake triggered many landslides on Haida Gwaii, and probably also triggered submarine landslides and local waves. The highest reported wave amplitude of about 3 m, documented in the Prince Rupert Daily News of August 27, 1949, was likely from a landslide-induced tsunami (Leonard et al., 2012).

From north to south along the Haida Gwaii margin, relative plate motion becomes increasingly oblique to the plate boundary, with an increasing component of convergence, although strike-slip motion still dominates (e.g., Hyndman, 2015). The oblique plate motion is partitioned between margin-parallel strike-slip earthquakes on the Queen Charlotte fault and less frequent margin-perpendicular thrust earthquakes on a separate subduction thrust fault that dips eastward beneath the islands (e.g., Hyndman, 2015). The Haida Gwaii thrust fault ruptured in October 2012 in a Mw 7.8 earthquake – this was the second largest instrumentally recorded earthquake in Canada, and the largest recorded thrust earthquake offshore British Columbia (Cassidy et al., 2014; Nykolaishen et al., 2015). The earthquake triggered a large tsunami, with run-up heights up to 13 m on western Haida Gwaii (Leonard and Bednarski, 2014). However, tsunami amplitudes were low at sites on eastern Haida Gwaii and elsewhere on the BC coast; the Prince Rupert tide gauge recorded a maximum wave amplitude of 13.9 cm (Fine et al., 2015). The mainland coast of northern BC, including Prince Rupert, was protected from direct wave impact because of the shadowing effect of Haida Gwaii and the directivity of the tsunami, which radiated energy westward from Haida Gwaii (Fine et al., 2015).

The 2012 Haida Gwaii earthquake involved a rupture length of ~150 km of the thrust fault offshore southern Haida Gwaii (Moresby Island); the thrust fault likely continues somewhat further north, but earthquakes with thrust mechanisms are expected to occur less frequently here than in the south, due to the lower convergence rate (Leonard et al., 2012; 2014). If rupture in a large thrust earthquake extends north of Haida Gwaii, a greater tsunami impact could be expected for the

northern mainland coast, including Prince Rupert, due to reduced shielding by the islands. Therefore, a source model for a subduction thrust earthquake extending north of Haida Gwaii is recommended, to investigate the potential tsunami impact.

Although the largest earthquake-sourced tsunamis originate at subduction zone plate boundaries, locally-hazardous waves can also be generated by earthquakes on shallow faults within the crust of an individual plate, either by direct displacement of the seafloor and/or by triggering of landslide-induced waves (e.g., >5 m maximum tsunami run-up from the 2016 Kaikoura, New Zealand crustal fault earthquake; Lane et al., 2017). In Hecate Strait between Haida Gwaii and the northern BC mainland, the presence of active crustal faults is indicated by a concentration of significant shallow seismicity, with earthquake focal mechanisms revealing a combination of thrust and strike-slip faulting (Ristau et al., 2007). Several structures have been mapped on the basis of geophysical data, including the Sandspit fault on the eastern side of Graham Island and several others to the east in Hecate Strait; none have been conclusively identified as active in historic or Holocene time, but the region remains poorly studied (e.g., Bustin, 2006).

In the absence of specific known tsunamigenic structures, Leonard et al. (2012; 2014) estimated the potential tsunami hazard of crustal faults in this area, based on the statistics of the earthquake catalogue and on the convergence rate across the region. They determined an approximate average recurrence interval of 730 years (270-1950 years) for potentially-tsunamigenic earthquakes of Mw 7.1 ± 0.3. Assuming pure thrust faulting and that a large earthquake is equally likely to occur anywhere within the Hecate Strait region, the probability of 1.5 m (or greater) tsunami wave run-up at any particular location on the mainland coast was estimated to be very low (~0.3-1.3% probability within a 50-year time period, or ~5000 years average recurrence). However, these estimates could be substantially higher for specific regions, if an optimally-located active structure was identified and modelled, and/or if potential landslide-triggered waves were accounted for. It is recommended that one or more scenarios be modelled, to investigate the potential tsunami impact from crustal fault and landslide sources.

The new source models recommended in this section can be coupled with the hydrodynamic model and this will help us to better understand and predict the tsunami wave behaviour, and how it may impact northern BC and nearby islands.

3. HYDRODYNAMIC METHODOLOGY

3.1 FUNWAVE-TVD

Starting with the vertical motions of the seabed of a given scenario, this is taken to be essentially instantaneous, and thus equivalent to the initial sea surface elevation. The 2DH Boussinesq wave model FUNWAVE-TVD is used to propagate this initial condition until it impacts upon the coastline. Such a fully nonlinear Boussinesq model can simulate more complete physics than a model based on the shallow water (i.e. Saint-Venant) equations, particularly dispersion, which is often important for properly computing coastal impact (Madsen et al., 2008). This model has been developed both as a fully nonlinear version in Cartesian coordinates (Shi et al., 2012), and a weakly nonlinear approximation in spherical coordinates (Kirby et al., 2013), and including the Coriolis effect. For this reason, to properly represent the physics of the problem as the wave approaches the coastline, it is

necessary to move between the two versions at different grid resolutions, discussed in the next section. Bottom friction is taken into account, using a constant Manning coefficient of 0.025 s/m$^{1/3}$, typical of a sandy seabed. Wave breaking is modelled by switching from the Boussinesq equations to the nonlinear shallow water equations when the wave height to depth ratio exceeds 0.8; in the simulations below, these limits are rarely achieved, except for a few grid cells near the coastline. The local Froude number is also limited to 2.0 to prevent numerical instabilities, though the Froude number rarely even exceeds one except for narrow constrictions in the flow, like in Fern Passage.

The FUNWAVE-TVD model has been used extensively for tsunamis around the world, including modelling of a potential flank collapse of the Cumbre Vieja Volcano in the Atlantic Ocean (Abadie et al. 2012), the 2011 Tohoku tsunami (Grilli et al. 2013), submarine mass failures along the US east coast (Grilli et al. 2015), interactions with tides (Shelby et al. 2016), and tsunami hazards in the Mediterranean (Nemati et al., 2018).
The model is also used for and benchmarked in the US NTHMP (National Tsunami Hazard Mitigation Program; Horrillo et al., 2014) for hazard mapping along the US coastline.

3.2 Nesting

A series of nested grids are used to propagate the potential tsunamis from the source regions up to the city of Prince Rupert, see Figure 1. The resolution increases in each grid by a factor or 4 or 6. The information transferred between each grid corresponds to the wave elevation and horizontal water velocity at each grid boundary, which is interpolated linearly in time and space. The details of these nested grids are discussed below (Table 1).

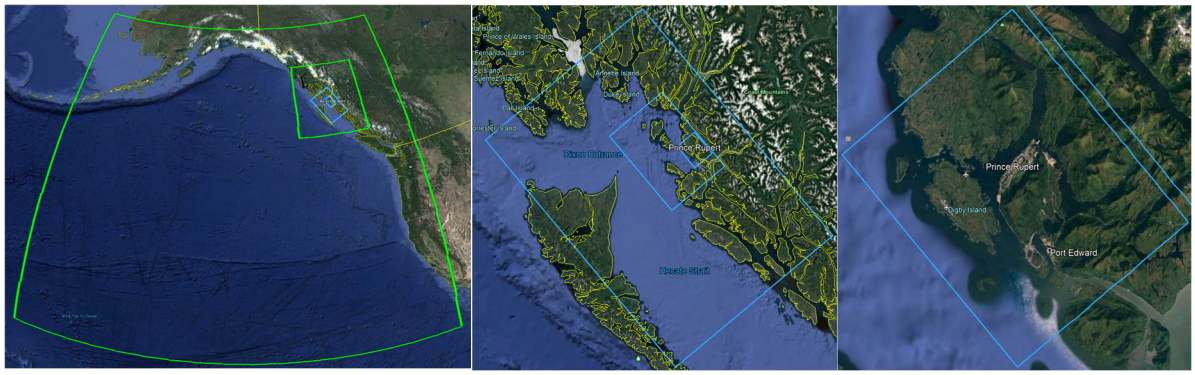

(a) (b) (c)

Figure 1: The view of nested grids. (a) The two outlines in green colour from outermost to the center are G0 and G1 with 2' and 30" resolutions, respectively; (b) The three outlines in blue color from outermost to the centre are G2, G3, and G4 with 240 m, 60 m, and 10 m resolutions, respectively; (c) The outline with blue colour at the centre is the finest nest G4 with 10 m resolution.

Table 1: Information of the numerical grids

Grid	Latitude	Longitude	Resolution	Size
Northeast Pacific (G0)	28° to 64°N	172° to 118°W	2 arc-minute	1621 x 1081
British Columbia (G1)	50° to 60°N	136° to 126° W	30 arc-second	1201 x 1201
Haida Gwaii (G2)	52.30° to 55.70° N	133.66° to 128.43° W	240 metres	901 x 1301
Local region (G3)	53.77° to 54.89° N	131.65° to 129.90° W	60 metres	1209 x 1701
Prince Rupert (G4)	54.13° to 54.46° N	130.60° to 130.06° W	10 metres	2371 x 2911

3.2.1 Spherical to spherical

An initial grid in spherical coordinates with a horizontal resolution of 2 arc-minutes is used for the initial source generation, which previous experience showed was necessary to reproduce tsunami waveforms in the Pacific with the FUNWAVE-TVD model (e.g., Kirby et al. 2013); significantly coarser resolutions would have undesirable numerical dispersion, and significantly higher resolutions would require significantly more computational time. 200 km thick absorbing sponge layers are applied to all boundaries to avoid non-physical reflections.

As the wave approaches the area of interest, higher resolution is required to capture the physics both as the wavelength decreases due to shoaling, and in order to capture the effect of the bathymetry.
A second spherical mesh at 30 arc-seconds resolution is used for the area covering most of the British Columbian coastline. No sponge layer is applied at the boundaries for these finer grids.

3.2.2 Spherical to Cartesian

In order to convert to a Cartesian mesh, a transverse Mercator projection was used. This is similar to a UTM projection, but with an origin located at 54° N, 131° W to minimize distortion to the grid as the wave propagates to the shore. This projection was used instead of a regular UTM project because Prince Rupert itself is at the western edge of UTM grid 9, so using an actual UTM projection would be problematic, as the waves arrive from the west (i.e. from outside of UTM grid 9). In order to better align the higher-resolution meshes with the coastline and continental shelf, and thus ensure that most of the grid cells are composed of the coastal region, a counterclockwise rotation of 30° between geographical coordinates and the numerical domain has been performed. This rotation implies that the velocity at the boundary conditions have been rotated by 30° to match the orientation of this new grid, and this projection of the velocities was applied to the stored data for the coupling between the two grids.

3.2.3 Cartesian to Cartesian

This result is then refined again two times, first to 60 m resolution, then 10 m. The 30° rotation is kept for each Cartesian grid so that the grid points correspond to the same locations in the next grid, and the origin of the transverse Mercator projection is kept as well.

3.3 Bathymetry and topography assimilation

Many different datasets were used to construct the bathymetry and topography required for the FUNWAVE-TVD simulations, making use of the best available bathymetry for each grid of the simulation. Each grid uses its own composition of bathymetry and topography data to ensure that the resolution used is as close as possible to the numerical grid spacing. Each dataset used is interpolated on the numerical grid. When several resolutions are integrated into one numerical grid

the highest resolution is prioritized. A summary of the datasets used (and their respective resolutions) is presented in Table 2.

Table 2: Summary of the datasets used for simulations

Dataset	Resolution
ETOPO1	1 arc-minute
British Columbia 3 arc-second Bathymetric Digital Elevation Model	3 arc-second
Southeast Alaska 8 arc-second MHHW Coastal Digital Elevation Model	8/15 to 8 arc-second
Canadian Digital Elevation Model (CA DEM)	20 metre
Electronic Navigational Charts, Canadian Hydrographic Service (CHS)	Various resolutions
Airborne Imaging of Calgary, Alberta, Canada, The City of Prince Rupert	1 metre
USGS NED Digital Surface Model AK Ifsar, United States Geological Survey (USGS)	5 metre
Prince Rupert Area Intertidal LiDAR, University of Northern British Columbia (UNBC)	1 metre

The following lists the datasets used for each grid:

- Northeast Pacific (G0):
  - ETOPO1
- British Columbia (G1):
  - ETOPO1
- Haida Gwaii (G2):
  - Southeast Alaska 8 arc-second MHHW Coastal Digital Elevation Model
  - British Columbia 3 arc-second Bathymetric Digital Elevation Model
  - ETOPO1
- Local region (G3):
  - Southeast Alaska 8 arc-second MHHW Coastal Digital Elevation Model
  - British Columbia 3 arc-second Bathymetric Digital Elevation Model
  - Canadian Digital Elevation Model (CA DEM)
  - Electronic Navigational Charts, Canadian Hydrographic Service (CHS)
  - Airborne Imaging of Calgary, Alberta, Canada, The City of Prince Rupert
  - USGS NED Digital Surface Model AK Ifsar, United States Geological Survey (USGS)
  - Prince Rupert Area Intertidal LiDAR, University of Northern British Columbia (UNBC)
- Prince Rupert (G4):
  - Canadian Digital Elevation Model (CA DEM)
  - Electronic Navigational Charts, Canadian Hydrographic Service (CHS)
  - Airborne Imaging of Calgary, Alberta, Canada, The City of Prince Rupert
  - USGS NED Digital Surface Model AK Ifsar, United States Geological Survey (USGS)
  - Prince Rupert Area Intertidal LiDAR, University of Northern British Columbia (UNBC)

After interpolation on the numerical grid, some discrepancies may appear. These take the form of outliers that are clearly out of the bounds of the actual topography in the region. Outlier points were excluded from each dataset before interpolation (e.g., 9000 m outliers in the CHS at 50 m resolution dataset, or an unrealistic gradient between two adjacent points). The sharp gradients that lead to numerical instabilities were thereby smoothed out.

We note that this issue is common when interpolating several datasets with varying resolution. In order to stay as close as possible to the bathymetry data provided, we ran each nest with unmodified data and we linearly smoothed only the regions that were leading to numerical instabilities. These regions are the following:

- G0:
  - None
- G1:
  - None
- G2:
  - None
- G3:
  - Shallow water region between 54.6°N and 54.62°N and 130.54°W and 130.52°W (figure 2a).
- G4:
  - The Pier between 54.28°N and 54.29°N and 130.365°W and 130.355°W (figure 2b).
  - Various locations around Prince Rupert. These smoothings were performed over the coastline and will not affect the simulations.

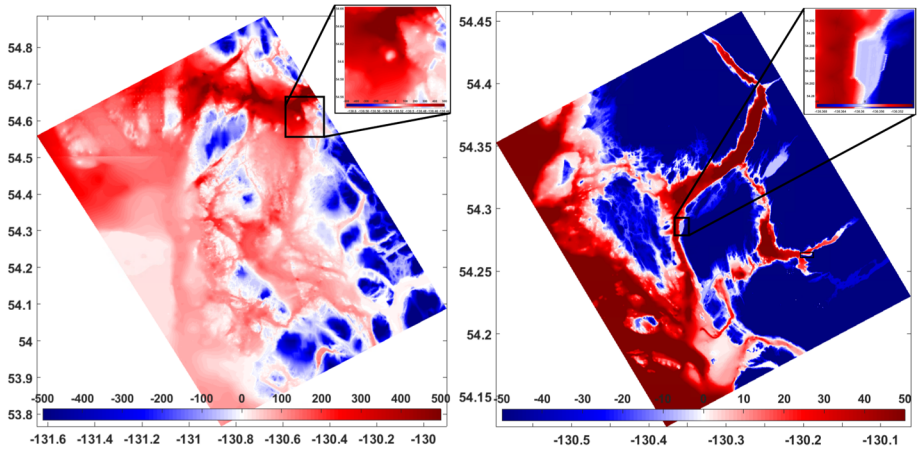

(a) (b)

Figure 2: Smoothed regions: (a) G3; (b) container terminal for G4. The bathymetry is positive and topography is negative.

All the regions with discrepancies that were not leading to instabilities were kept in the numerical experiment (e.g., the line between 131.5°W and 131.0°W at 54.5°N in G3; see Figure 2a).

3.4 Future sea-level rise

Recent research shows that sea-level rise can significantly increase the tsunami hazard, and even minor sea-level rise, can pose greater risks of tsunamis for coastal communities worldwide. In this regard, Li et al. (2018) developed probabilistic tsunami inundation maps by using an extensive Monte Carlo tsunami inundation simulation for a case study for Macau located on the south coast of China. They showed that 0.5 m sea level rise by 2060 will double the tsunami hazard. Also, their results indicate that conservative amount of 1.0 m sea level rise by 2100 can dramatically increase the frequency of tsunami-induced flooding incidence by a factor of 1.5 to 4.7.

Adding 1.0 m to account for sea-level rise by 2100 is the guidance of the MFLNRO Coastal Floodplain Mapping Guidelines and Specifications. Regional studies suggest that this corresponds to an extreme but not unrealistic condition. The inclusion of the sea-level rise is simply by adjusting the bathymetry in our numerical experiment by 1.0 m.

4. RESULTS

4.1 Initial source selection

4.1.1 Alaska-Aleutian subduction zone

For all three source models previously outlined for the 1964 tsunami (Johnson et al., 1996; Ichinose et al., 2007; Suito and Freymueller, 2009), at first, a low-resolution run was considered, making use of the vertical motions to provide initial conditions. The maximum uplift and subsidence for these three different sources are shown in Table 3.

Our low-resolution tsunami simulation indicates that the results of the source model by Johnson et al. (1996) generate a higher maximum tsunami height compared to Ichinose (2007) and Suito and Freymueller (2009) in the Prince Rupert area as shown in Figure 3. The vertical displacement of seafloor based on the source model by Johnson et al. (1996) which is used for the experiments is illustrated in Figure 4. In order to best represent the risk to the city, based on our available dataset, this source is retained for high-resolution modelling below.

Table 3: Maximum uplift and subsidence for Alaska subduction zone

Alaska Subduction Zone	Max Uplift (+)	Max Subsidence (-)
Johnson et al. 1996	6.86 m	-5.47 m

Ichinose et al. 2007	8.60 m	-1.81 m
Suito and Freymuller 2009	2.78 m	-1.80 m

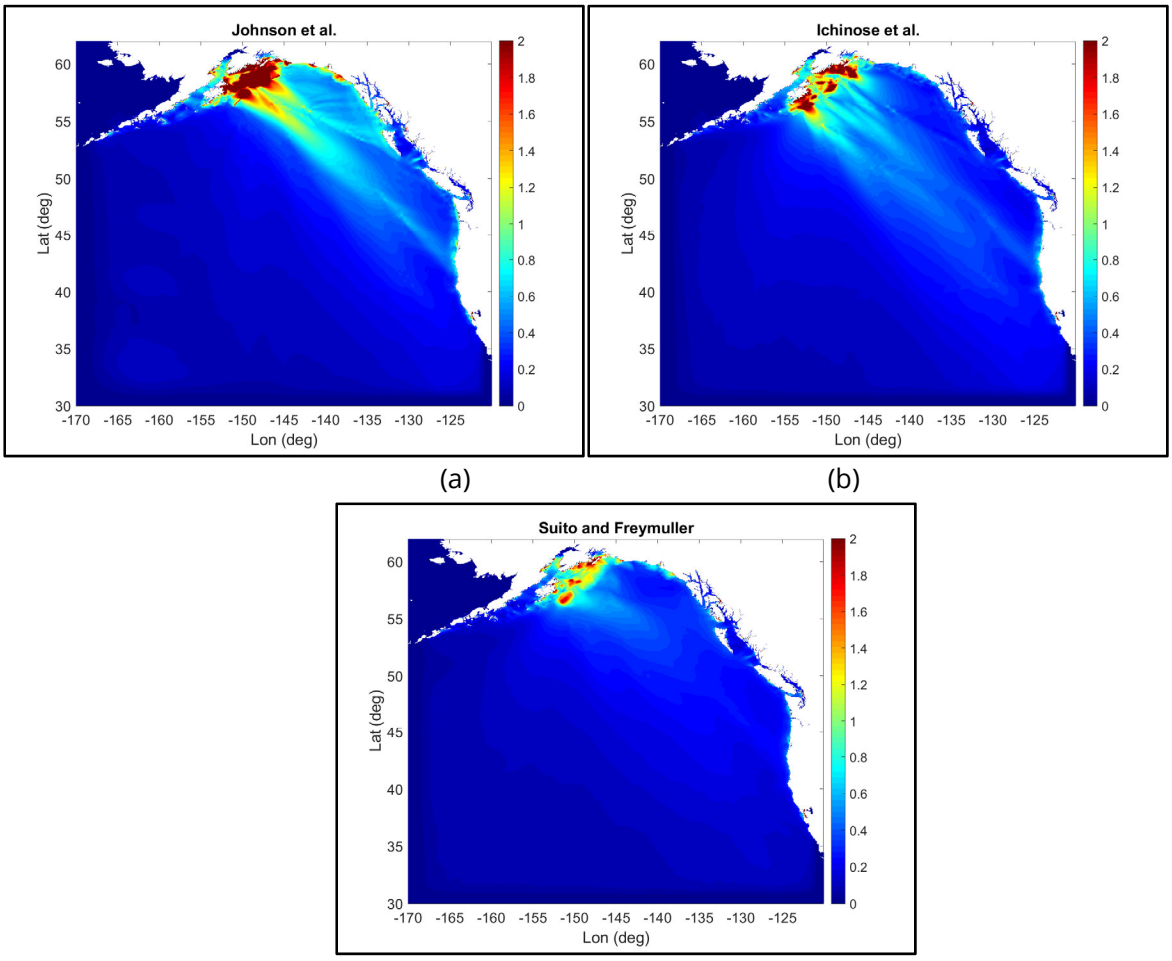

Figure 3: Maximum tsunami height (m) based on low-resolution simulation for the 1964 Alaska subduction zone earthquake using three different source models: (a) Johnson et al.1996; (b) Ichinose et al. 2007; (c) Suito and Freymuller 2009.

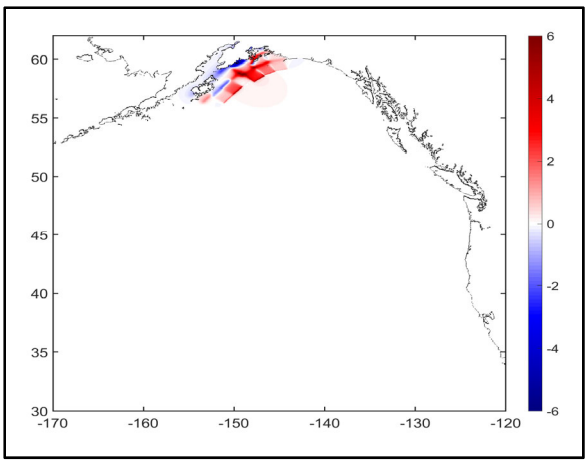

Figure 4: Seafloor vertical displacement (m) at the source region for the 1964 Alaska subduction zone earthquake based on the source model by Johnson et al. (1996).

4.1.2 Cascadia subduction zone

For this case, we consider four different scenarios from Gao et al. (2018): a buried rupture, a splay-faulting rupture, full trench-breaching rupture and half trench-breaching rupture. The maximum uplift and subsidence for these three different sources are shown in Table 4.
Similar to the Alaska subduction zone, the low-resolution tsunami simulation indicates that splay fault rupture can generate higher surface elevation compared to the buried, half and full trench ruptures (Figure 5). Therefore, in the following section, the splay faulting scenario will be retained as the primary. The vertical displacement of the seafloor for this scenario is illustrated in Figure 6.

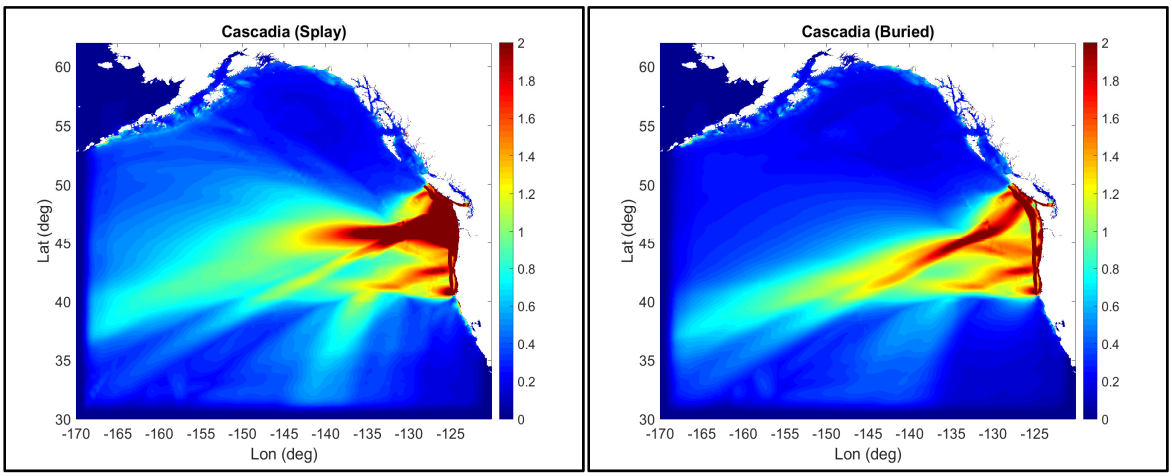

(a) (b)

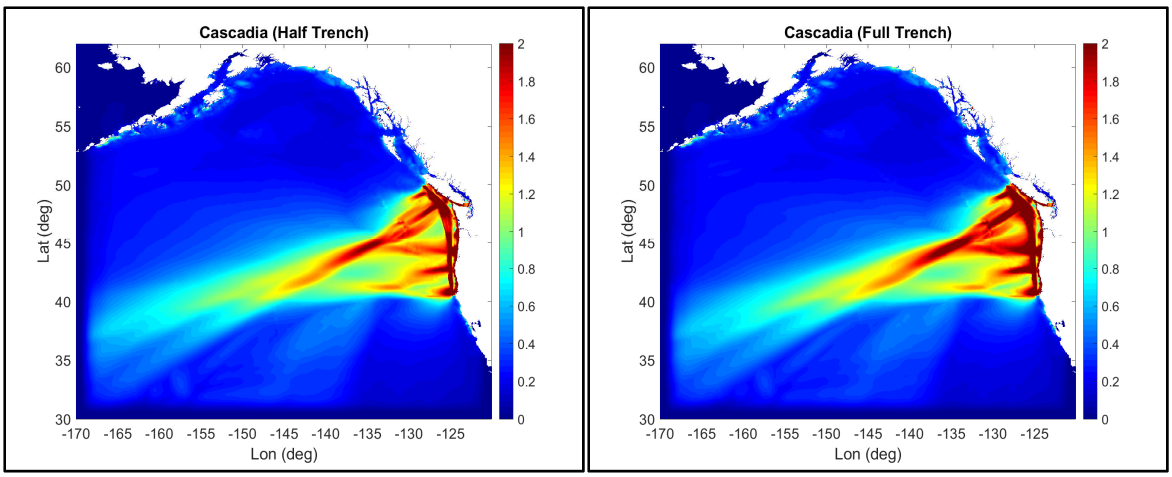

(c) (d)

Figure 5: Maximum tsunami height (m) based on low-resolution simulation for Cascadia subduction zone earthquakes using four rupture scenarios: (a) Splay-faulting; (b) Buried rupture; (c) Half trench-breaching; (d) Full trench-breaching.

Table 4: Maximum uplift and subsidence for Cascadia subduction zone

Cascadia Subduction Zone	Max Uplift (+)	Max Subsidence (-)
Splay rupture	9.76 m	-2.60 m
Buried rupture	5.13 m	-2.63 m
Full-trench rupture	9.80 m	-2.63 m
Half-trench rupture	8.62 m	-2.62 m

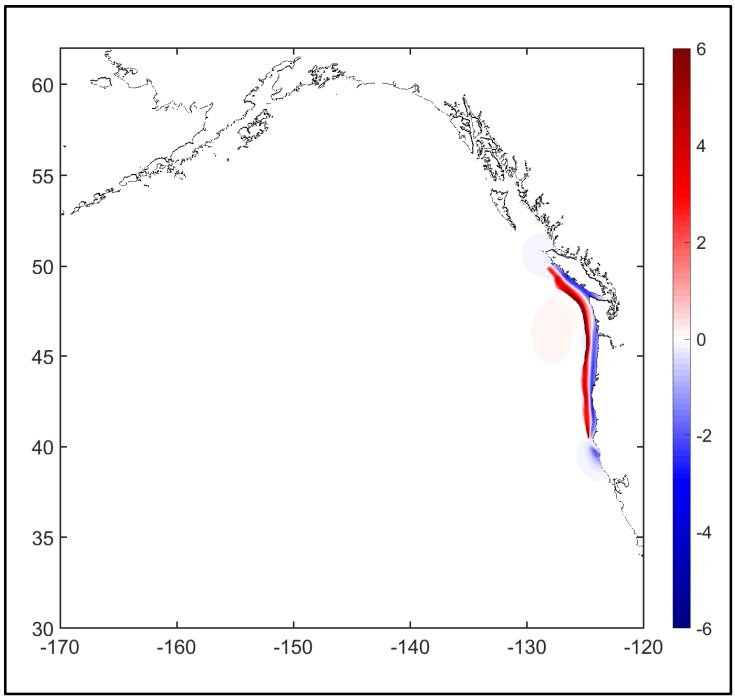

Figure 6: Seafloor vertical displacement (m) for the Cascadia subduction zone earthquake based on the splay rupture model (Gao et al., 2018).

4.2 Propagation from the source to Prince Rupert

Taking the two chosen sources, the Alaska-Aleutian subduction zone event (Johnson et al. 1996) and the Cascadia splay-faulting event (Gao et al. 2018), these are next simulated on the large-scale grids for a duration of 24 hours. Special care is taken at this stage to ensure that the initial free-surface elevation takes into account the horizontal motion of the seabed, which can be important, particularly around the Alaskan coastline where there are sharp slopes in the bathymetry.
As mentioned above, this is first done on a grid from 28° to 64°N and 172° to 118°W, with a 2' resolution, and 200 km thick sponge layers on all sides to prevent reflections, then a grid from 50° to 60°N and 136° to 126°W, with a 30" resolution, again using initial conditions from the tsunami sources, as the Cascadia source region is large enough to overlap slightly with the boundaries of G1. Finer Cartesian grids, at 240 m, 60 m, and 10 m, are further away from the sources, and therefore start at rest. For the nests 0 to 3, the wave amplitudes are presented in respect with the mean sea-level. This reference has been adjusted in the last nest (Region of Prince Rupert) to the Mean Higher High Water (MHHW) which has been previously evaluated to 2.3m above mean sea level based on the available tidal gauge in this region (Fine et al. 2018a, 2018b).

4.2.1 Alaska-Aleutian subduction zone

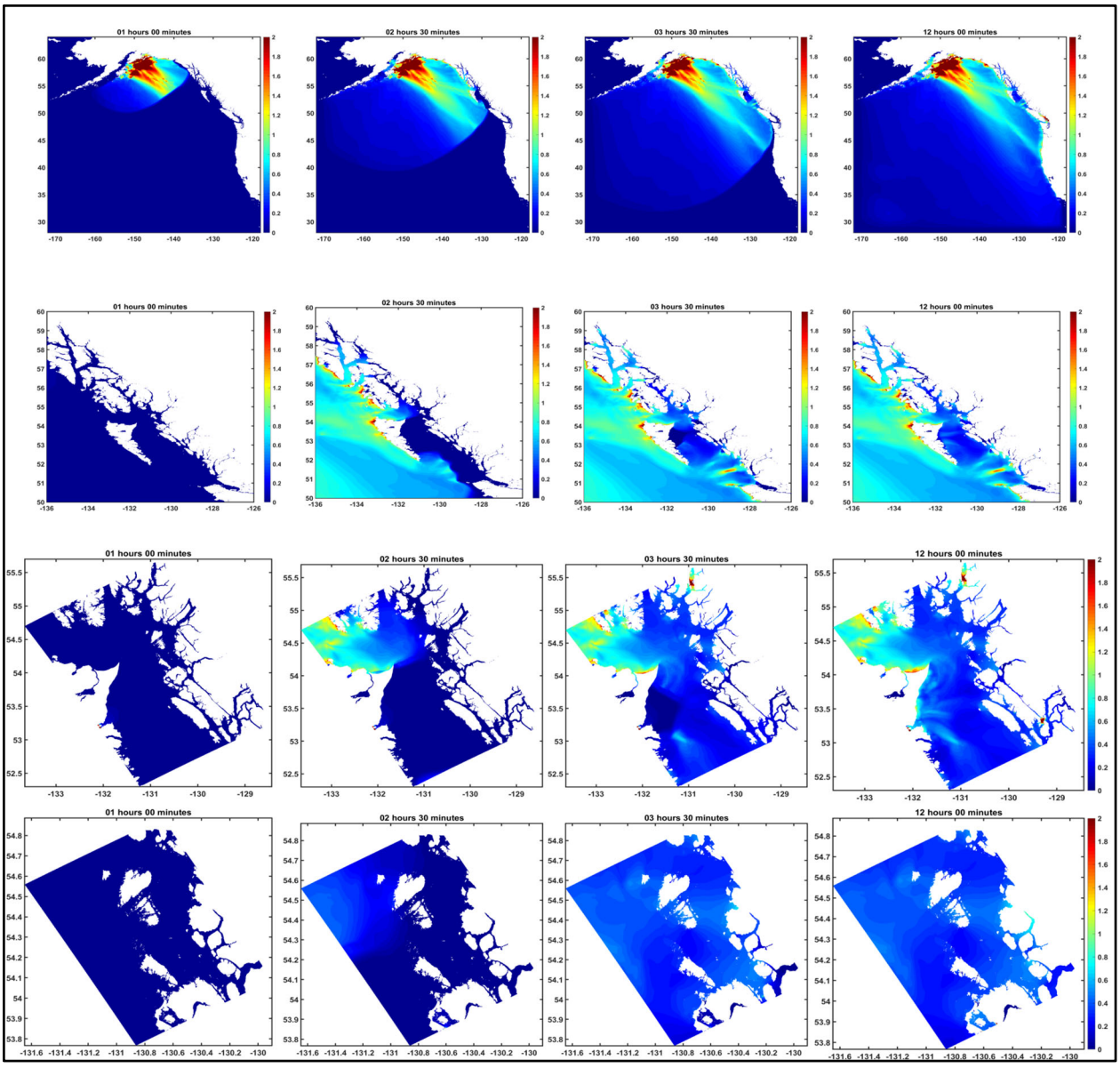

(a) (b) (c) (d)

Figure 7: Maximum tsunami wave height for the Alaska-Aleutian event at different times for different grids. (a) t = 1h00 (b) t = 2h30 (c) t = 3h30(d) t = 12 hours. First, second, third, and fourth rows from the top to the bottom are representing the G0, G1, G2, and G3 grids, respectively.

Figure 7 shows the maximum wave height at different time steps (t = 1 hour, t = 2 hours, t = 3 hours, t = 12 hours; from left to right), from G0 (first line) to G3 (fourth line). We observe that the tsunami properly transmit from one nest to the next one, and reaches the Prince Rupert region (nest 4) in approximately 3 hours.
The detailed propagation of the wave amplitude for each nests from when the earthquake occurs to 8 hours is shown in Annexe A.

4.2.2 Cascadia subduction zone

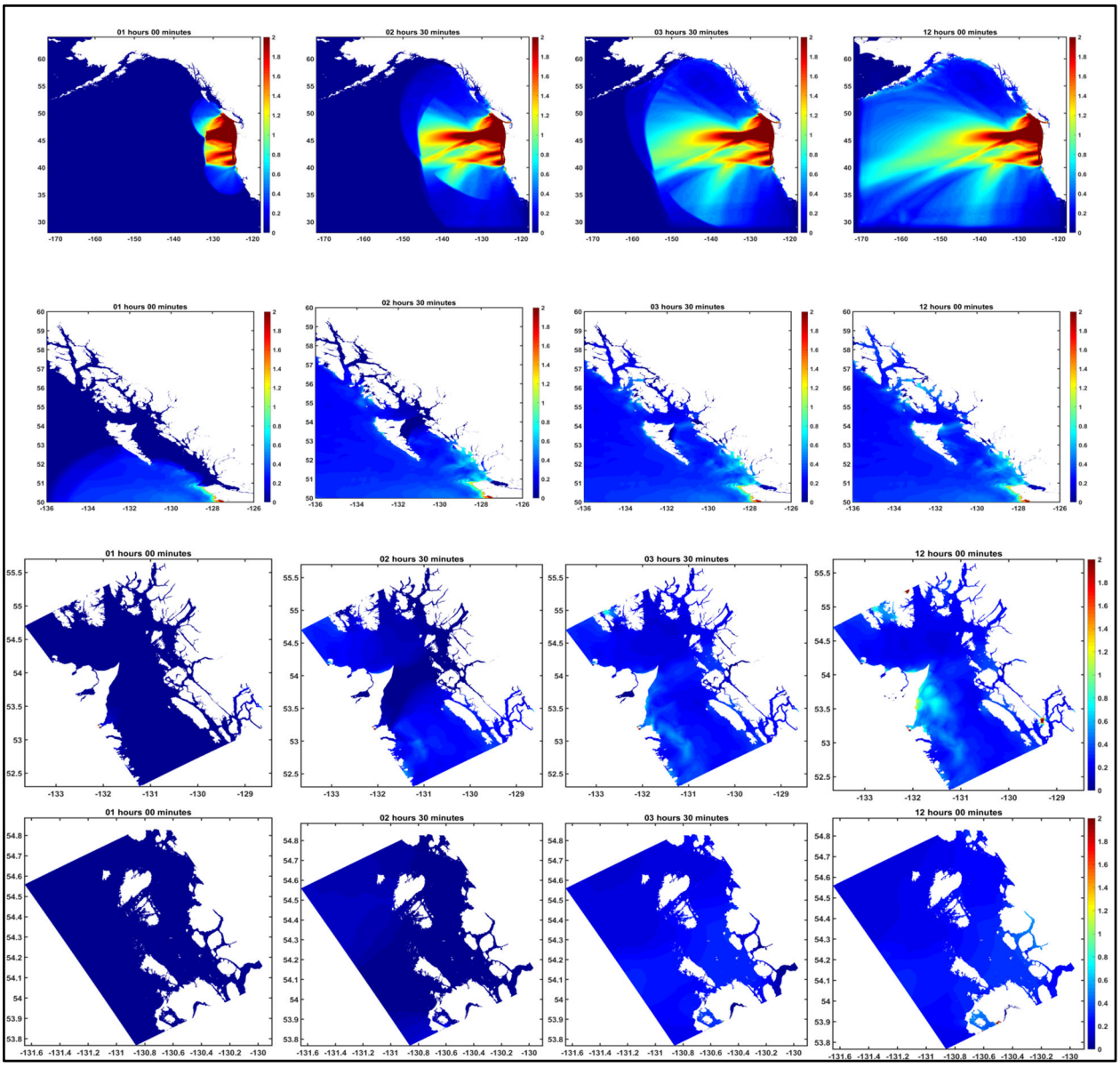

(a) (b) (c) (d)

Figure 8: Maximum tsunami wave height for the Cascadia subduction zone event at different times for different grids. (a) t = 1h00 (b) t = 2h30; (c) t = 3h30 (d) t = 12 hours. First, second, third, and fourth rows from the top to the bottom are representing the G0, G1, G2, and G3 grids, respectively.

Figure 8 shows the maximum wave height at different time steps (t = 1 hour, t = 2 hours, t = 3 hours, t = 12 hours; from left to right), from G0 (first line) to G3 (fourth line). We observe that the tsunami properly transmits from one nest to the next one, and reaches the Prince Rupert region (nest 4) in approximately 3 hours and 30 minutes.

The detailed propagation of the wave amplitude for each nest from when the earthquake occurs to 8 hours is shown in Annexe B.

We note that the unusual wave height in the southeast part of G2 is related to numerical instabilities that do not propagate towards G3, and thus, towards Prince Rupert. Consequently, it does not impact our results.

4.2.3 Detailed Comparison of the tsunami wave timing

A more detailed comparison between arrival times and variation of amplitudes close to Prince Rupert was performed. We added a numerical tide gauge at 54°19'2" N, 130°19' 28" W and observed the water elevation starting when the earthquake occurs (Figure 9) for both cases.

Alaska's earthquake generates the first tsunami wave amplitude about 0.5 m which reaches this tide gauge at Prince Rupert 3 hours and 40 min after the earthquake. After 5 hours and 30 minutes follows a second wave that has a higher maximum wave peak at 1 m. The following waves have a decreasing amplitude with a period of about 2 hours (not shown after 12 hours).

Cascadia's earthquake generates an initial tsunami of about 0.5 m height which reaches this tide gauge at Prince Rupert around 4 hours after the earthquake. This is the maximum wave height that reaches this location, the following waves have a decreasing amplitude with a period of about 100 minutes (not shown after 12 hours).

Based on the seismic source models which have been used in this study, the Alaska subduction zone can produce larger wave height compared to the Cascadia case, and the maximum tsunami wave which will hit Prince Rupert is predicted to be about 1 m in amplitude. For a better quantitative comparison, the values of wave amplitude including the first wave, maximum crest and trough with their arrival time for both sources are presented in Table 5.

It should be stressed that here we have discussed the tsunami wave amplitudes, periods, and arrival times for one specific point. However, for a better judgment of the tsunami impact to the coastal areas, the distribution of the maximum wave heights and current velocities also needed to be considered along with a greater number of specific locations.

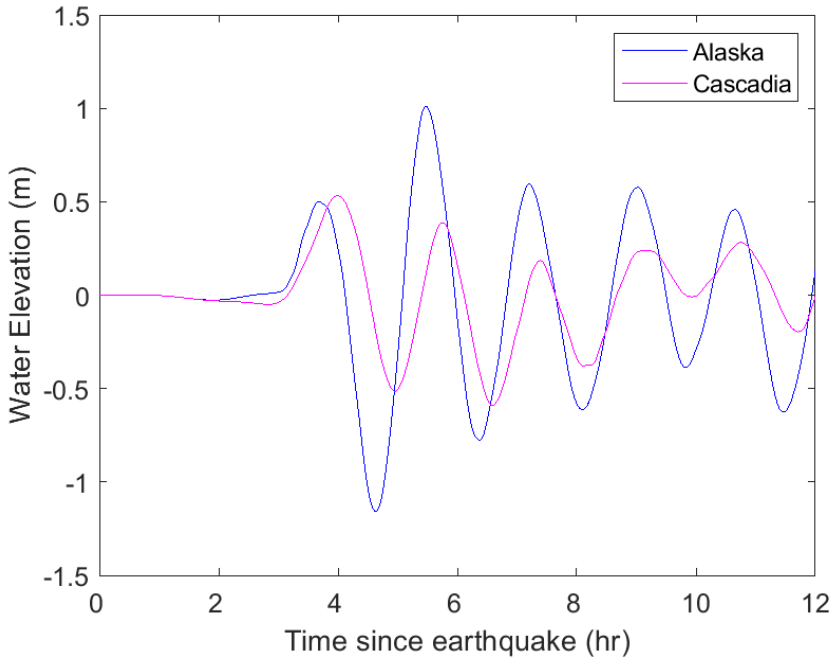

Figure 9: Comparison of the modelled water elevation for Alaska and Cascadia earthquakes at a numerical tide gauge in Prince Rupert at 54°19'2" N, 130°19' 28" W.

Table 5: Tsunami wave amplitude and its arrival time for Alaska 1964 and Cascadia sources at the station location.

Source model	First wave (+)		Maximum crest (+)		Maximum trough (-)	
	Amplitude	Arrival time	Amplitude	Arrival time	Amplitude	Arrival time
Alaska	0.5 m	3 h 40 min	1 m	5 h 30 min	- 1.16 m	4 h 37 min
Cascadia	0.53 m	4 h	0.53 m	4 h	- 0.59 m	6 h 35 min

4.3 Prince Rupert: High-resolution modelling

In the final grids, the dispersive terms, interacting with bathymetry which had not been smoothed in order to respect the dataset provided, were leading to numerical noise and break-down of FUNWAVE-TVD. As a result, these terms were turned off in G4 only, therefore modelling with nonlinear shallow water (i.e., Saint-Venant) equations, for this grid. This may slightly alter very short waves that can appear but should not significantly impact the main wave, nor propagation of the tsunami around Prince Rupert. A map showing the key regions we are going to discuss in this section is shown in Annexe C.

Since we consider two different seismic sources including Alaska 1964 event and Cascadia subduction zone event, the assumption of the simulation for the present date and the future time with 1 m sea-level rise, will require four scenarios to be simulated for this project. The information on these different scenarios is presented in Table 6. The present time is corresponding to the year 2019 without the sea level rise, while the future time is corresponding to the year 2100 and it is

assumed that the sea level rises about 1 m in comparison to the present time. The adjustment in the sea-level is performed in in Prince Rupert region only (nest 4).

Table 6: Information for different scenarios.

Scenario	Source	Time	Year	Sea level rise
1	Alaska 1964	Present	2019	-
2	Cascadia (Splay)	Present	2019	-
3	Alaska 1964	Future	2100	1 m
4	Cascadia (Splay)	Future	2100	1 m

4.4 Discussions for different scenarios

4.4.1 Present day

Under the present day conditions, the numerical experiment shows a maximum wave height of about 1.5 m above the MHHW level with an earthquake from the Alaska zone (Figure 10) and of about 0.8 m with an earthquake from the Cascadia zone (Figure 11). In both cases, the maximum height occurs inside Tuck Inlet, with a maximum height at the end of the inlet, decreasing towards the city of Prince Rupert. At the easternmost side of Prince Rupert (offshore of Seal Cove), the wave height is about 1.1 m in the Alaska case and 0.8 m in the Cascadia case. On the west side, close to the BC Ferry Terminal, the wave height is about 0.6 m in the Alaska case, and 0.4 m in the Cascadia case. We note that in this region there is an abrupt transition in the wave height, from a height of about 0.4 m south of BC Terminal to 1.0 m north of the port in the Alaska case, and from 0.3 to 0.6 m in the Cascadia case.

High wave induced velocities are present into two channels around Digby Island and close to Seal Cove due to the significant wave height gradient. The velocities are up to 3.0 m/s and 4.0 m/s, respectively, in the Alaska case. In the Cascadia case, the velocities are up to 1.0 m/s and up to 1.8 m/s for the same areas, respectively.

The overall distribution of wave amplitude is consistent with Fine et al. (2018a) and Fine et al. (2018b) who obtained similar values for the region of Prince Rupert. At the exact same location of the station used in Fine et al. (2018a, 2018b) our experiments present a difference in wave height and velocity of 20% on average and locally up to 35% lower than their study. However, these differences can be explained by a difference in the bathymetry and topography data used, as well as the different resolution between our study and theirs, especially when the highest differences are compared with local stations.

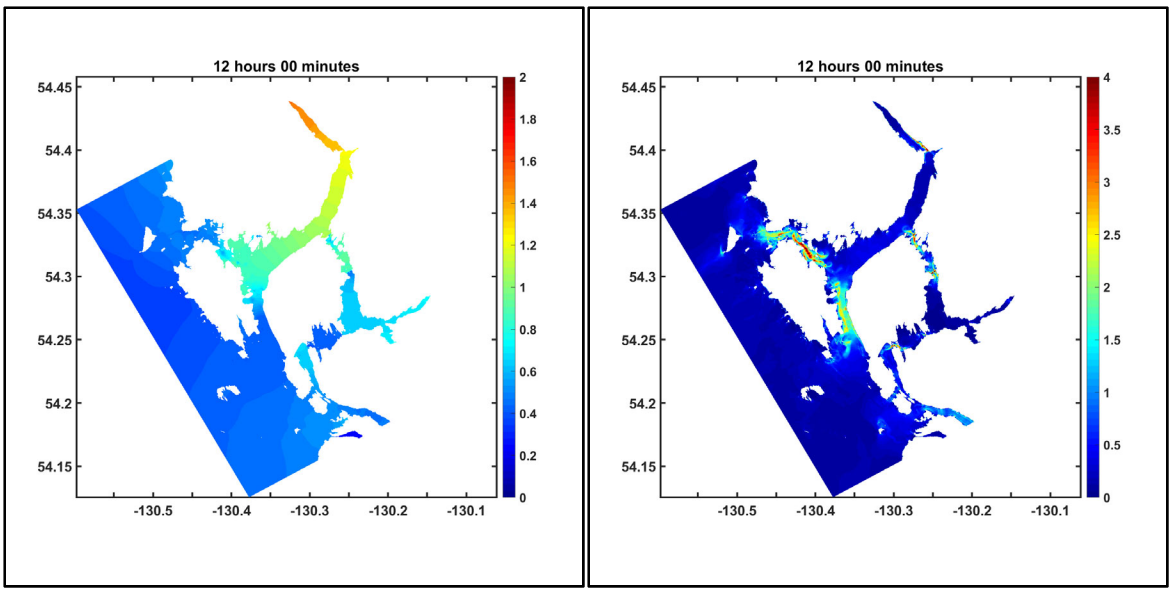

(a) (b)

Figure 10: Scenario 1 (Alaska-Aleutian event): (a) Maximum wave height (m) after 12 hours; (b) Maximum velocity (m/s) after 12 hours.

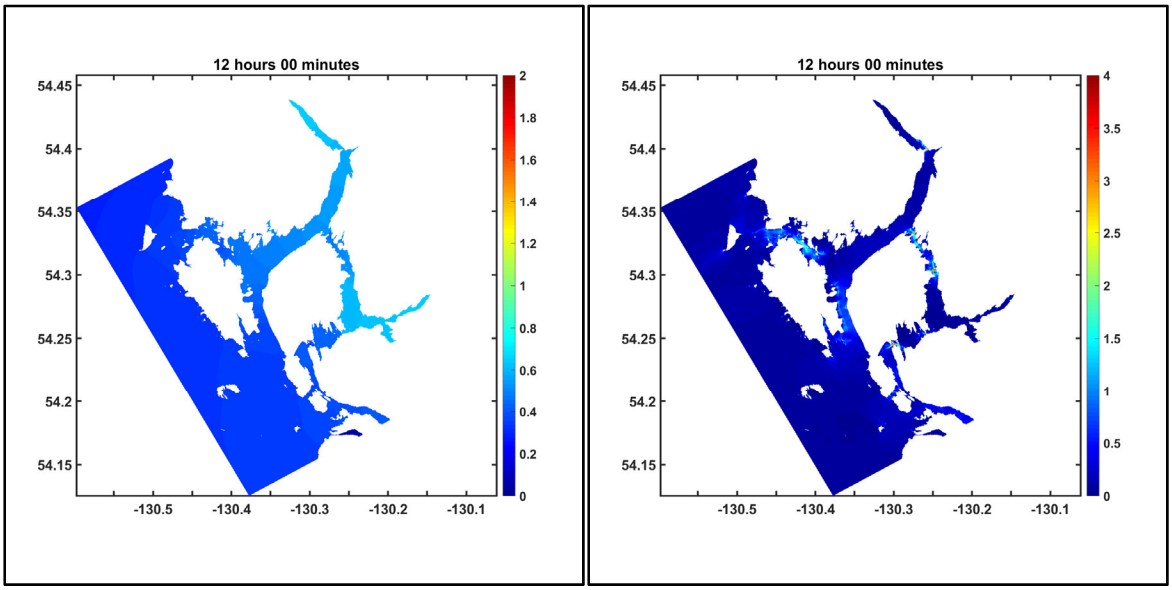

(a) (b)

Figure 11: Scenario 2 (Cascadi event): (a) Maximum wave height (m) after 12 hours; (b) Maximum velocity (m/s) after 12 hours.

4.4.2 Specific locations of high interest

To further compare and evaluate the tsunami wave height and velocity at important coastal areas, six specific locations corresponding to different Ferry terminals and marinas are selected. These locations include Airport Ferry (station 1), Digby Island Ferry (station 2), Metlakatla Marina (station 3), Cow Bay Marina (station 4), Port Simpson Ferry (station 5), and Lax Kw'Alaams Ferry (station 6).

The information for these stations and their coordinates is presented in Table 7. The locations of these stations in the computational domain are shown in Figure 12.

Table 7: Localisation of each station

Station	Location	Longitude (°W)	Latitude (°N)
1	Airport Ferry	130.3547	54.2941
2	Digby Island Ferry	130.4028	54.3130
3	Metlakatla Marina	130.4348	54.3396
4	Cow Bay Marina	130.3213	54.3193
5	Port Simpson Ferry	130.2831	54.3336
6	Lax Kw'Alaams Ferry	130.3144	54.4336

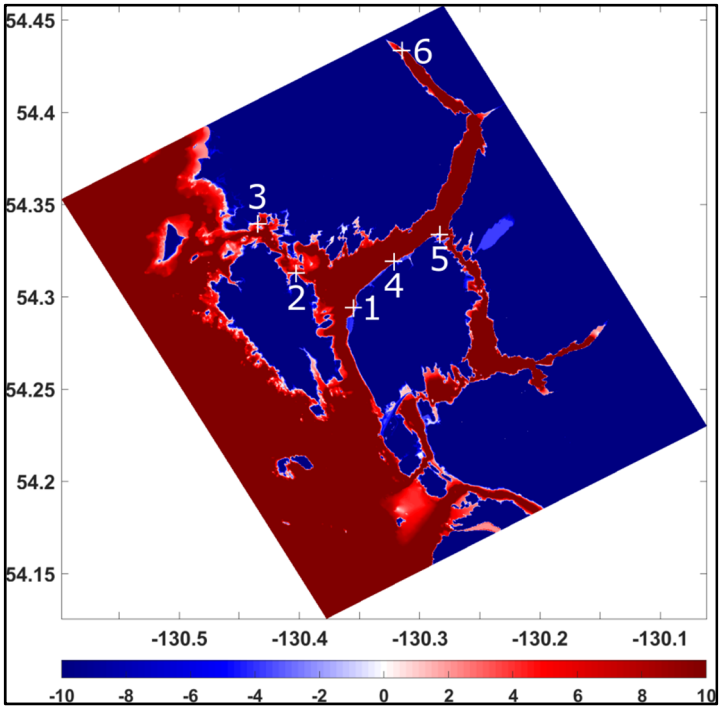

Figure 12: Locations of six selected stations in the Prince Rupert region. The bathymetry is positive and topography negative.

The time series of the tsunami wave height and tsunami-induced currents for the selected stations are shown in Figures 13 and 14, respectively. As is expected and discussed in the previous section, the Alaska test case generated higher tsunami waves compared to the Cascadia case. Therefore, the tsunami wave for this case (scenario 1) is discussed in this section. Figure 13 shows that the maximum wave amplitude is predicted near to 1.5 m at Lax Kw'Alaams Ferry, located in Tuck inlet, which has higher wave amplitudes compared to other stations.

The maximum wave amplitude at Port Simpson Ferry (station 5) located in Seal Cove is about 1 m, which is relatively similar to the maximum amplitude at Cow Bay Marina (station 4) in the Prince Rupert Harbour, although its maximum trough is 1.3 m deep is slightly larger than the maximum trough at Cow Bay Marina (1.1 m deep). The maximum wave height toward the south of Prince Rupert Harbour at Airport Ferry (station 1) is estimated with smaller amplitude around 0.8 m which would be less than the tsunami height of 1 m at Prince Rupert harbor.

The maximum total wave amplitude from peak to trough for the Digby Island Ferry (station 2) and Metlakatla Marina (station 3) farther west of Kaien Island are 1.78 m (from -1 to 0.78 m) and 1.28 m (from -0.78 to 0.5 m), respectively. These amplitudes are smaller compared to the wave amplitudes at Prince Rupert region.

The comparison of wave induced currents are illustrated in Figure 14. In agreement with the higher wave total amplitudes, the maximum wave induced currents are higher in the Alaska case (Scenario 1) compared to the Cascadia case (Scenario 2). The maximum wave velocity at Digby Island Ferry (station 2) can reach 3 m/s, which may represent a threat for navigation close to the harbor. On Kaien Island, the maximum currents are smaller, with a velocity less than 1 m/s at Prince Rupert Harbor, Cow Bay Marina and Port Simpson (station 1, 4 and 5). Finally, at Lax Kw'Alaams Ferry (station 6), despite having the highest modelled wave amplitude compared to other stations (1.5 m), the wave induced currents are the lowest (< 0.1 m/s).

These results at specific locations are not exactly similar in term of wave amplitude or wave induced currents with the overall impact of the tsunami wave on each region we discussed in the section 4.4.1. Locally, a lower or higher tsunami impact may occur (e.g., at station 1 versus "BC Terminal"). This is because the way the model represents the wave locally depends much more on the bathymetry in this exact location and immediate surrounding. Overall, the results at each stations are consistent with the large scale impact of the tsunami waves.

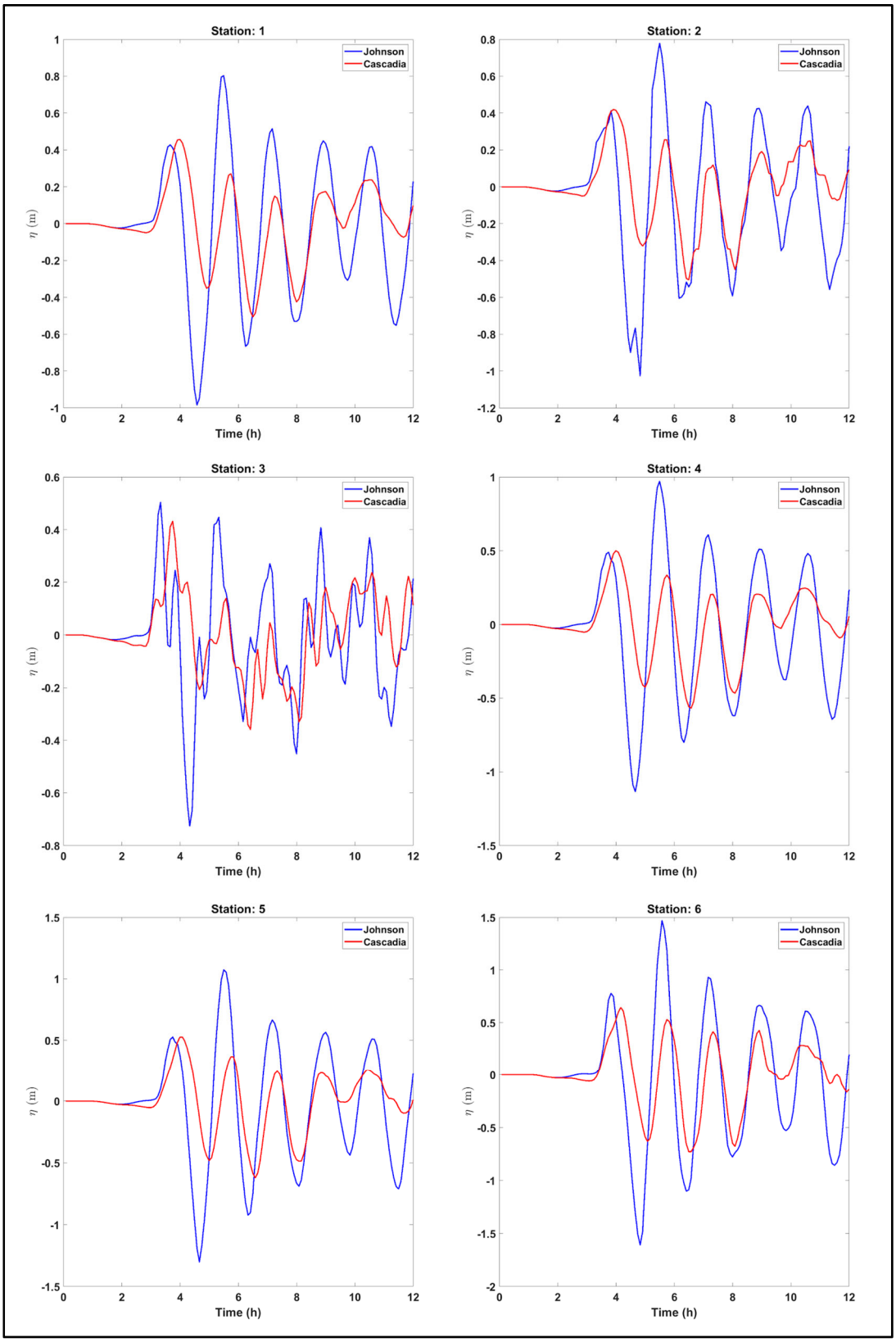
Station: 1
Johnson
Cascadia
η (m)
Time (h)
Station: 2
Johnson
Cascadia
η (m)
Time (h)
Station: 3
Johnson
Cascadia
η (m)
Time (h)
Station: 4
Johnson
Cascadia
η (m)
Time (h)
Station: 5
Johnson
Cascadia
η (m)
Time (h)
Station: 6
Johnson
Cascadia
η (m)
Time (h)

Figure 13: Tsunami wave height for Alaska-Aleutian (Johnson) and Cascadia events at stations presented in Table 7. Note that to see more clearly the variations at each location the y-axis varies on each panel.

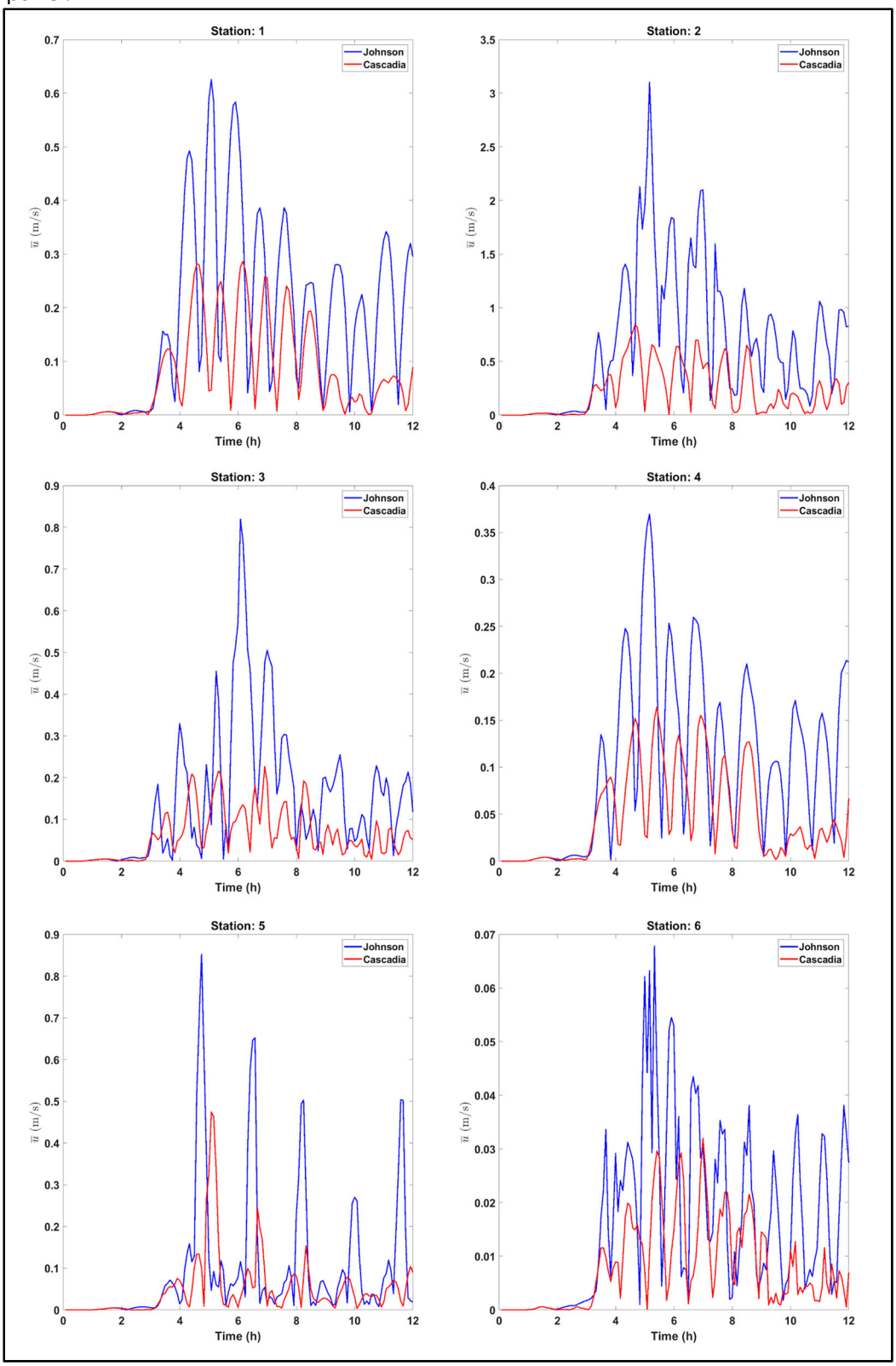

Figure 14: Wave induced current total velocities ($\bar{u} = \sqrt{(u^2 + v^2)}$) for Alaska-Aleutian (Johnson) and Cascadia events at stations presented in Table 7. Note that to see more clearly the variations at each location the y-axis varies on each panel.

4.4.3 Climate change

The addition of 1 m sea-level rise does not significantly impact the overall tsunami wave behaviour in any of the considered cases (Figure 15-16). Locally, in Fern Passage for the Johnson case, the climate change experiment shows a wave height of about half the height of the present day experiment (about 0.6 m). This is explained by the topography that is preventing the incoming wave from Tuck Inlet to pass the shallow water between Sea Cove and Fern Passage in this case.

Despite the small change in the wave propagation and amplitude with respect to present day, we note that this sea-level rise may have a significant impact on the tsunami run-up and coastal inundation. In this case, a wave of 1.1 metres corresponds to a wave of 4.4 metres above current mean sea level (1.1 m amplitude + 2.3 m MHHW adjustment + 1 m climate change), which can significantly impact the community of Prince Rupert.

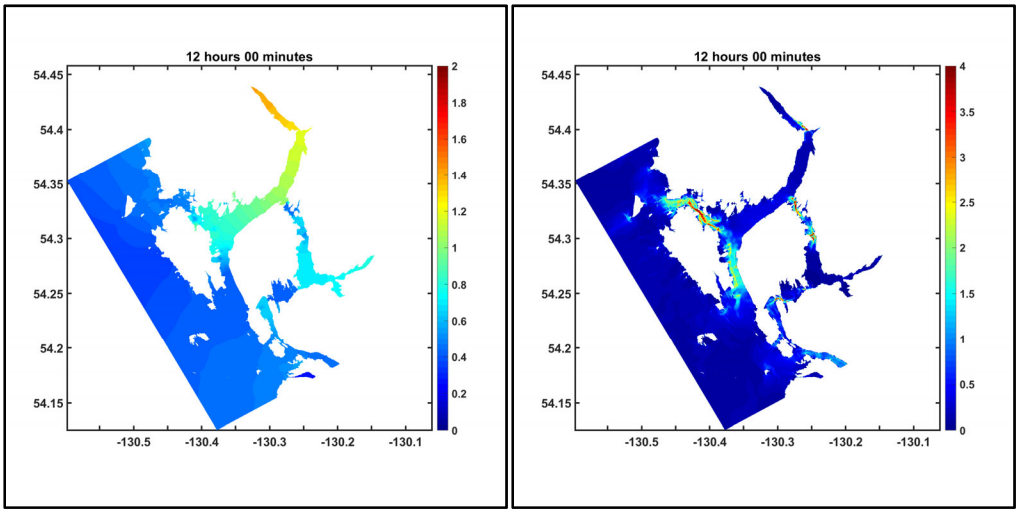

(a) (b)

Figure 15: Scenario 3 (Alaska-Aleutian event with climate change): (a) Maximum wave height (m) after 12 hours; (b) Maximum velocity (m/s) after 12 hours.

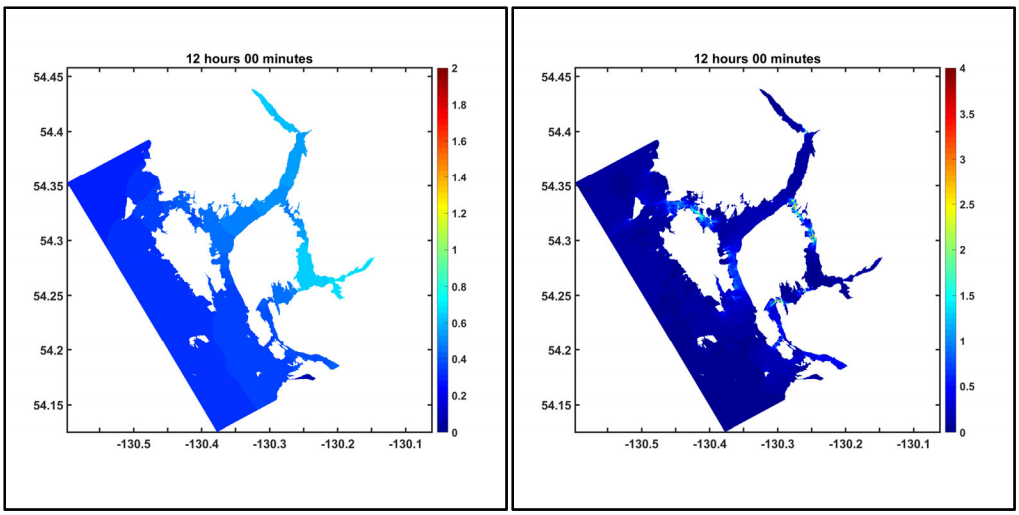

(a) (b)

Figure 16: Scenario 4 (Cascadia event with climate change): (a) Maximum wave height (m) after 12 hours; (b) Maximum velocity (m/s) after 12 hours.

5. SUMMARY

The tsunami hazard of the city of Prince Rupert from deterministic modelling appears to show that the 1964 tsunami, one of the largest tsunamis recorded, is representative of the largest risks due to co-seismic sources for the city of Prince Rupert. While a massive Cascadia tsunami would be devastating elsewhere, the wave height would actually be more modest at Prince Rupert. These results appear to be consistent with earlier results by Fine et al. (2018a, 2018b) who looked at tsunami hazard to the Prince Rupert coast guard station. We note that it was necessary to turn off the dispersion terms of the model at the finest level of resolution in the simulations, but this should not have any effect on the physics of the main incoming waves, as the wavelength is extremely long, and for this coastline the somewhat narrow shelf and deep inlets into the harbour do not seem to generate significant dispersive bores. In addition, the Manning coefficient is assumed to be constant over the entire domain (set to be equal to the one over sand). This coefficient in reality varies based on the roughness of the seabed. This coefficient might not influence the propagation of the wave in the deep ocean, but may be more important for the nearshore predictions.

The effect of sea-level rise does not appear to change the results substantially; that is, the tsunami wave height is similar at a larger sea level. This is somewhat expected as the water even at the harbour is quite deep; recall also that the tidal range in Prince Rupert is quite large and no significant differences are present between the experiments referred to MSL and MHHW.

While the results here did not exactly reproduce the 1964 tsunami, they do agree quite well for the first wave and the drawdown after. Detailed study of the following wavetrain requires additional work to analyze the available data; in addition to uncertainty in bathymetry or model parameters, previous works have shown substantially different tsunami records, depending on how the tidal signal was removed (e.g., Dunbar et al.,1988). In any rate, the dynamics of the individual waves was quite consistent with measurements and other simulations, including a significant drawdown after the initial wave, a higher wave height to the east of the city, and that the first wave is not necessarily the largest to impact the city.

For future work, it would be extremely useful to better integrate the bathymetry of the area into gridded DEMs with higher resolution (1 to 5 m) to run the tsunami modelling at higher resolutions. Differences between the depths at different grid resolutions posed a significant challenge for fixing the boundaries between each level of nesting in the simulations, and non-physical outliers had to be removed and sharp gradients smoothed (e.g., LIDAR data for the city of Prince Rupert indicated that a ship at the container terminal was a positive elevation, whereas this would normally be open water). These changes have no significant impact on the large scale experiments, but locally may lead to under or overestimation of the tsunami height and wave induced current velocity. Moreover, for this study, we considered only distant seismic sources. In addition, for a complete evaluation of the risks in the Prince Rupert region, local tsunami sources closer to Prince Rupert need to be investigated, e.g. landslides and earthquakes in the Haida Gwaii and Hecate Strait regions.

Given the limitations of this study, a safety factor such as that proposed by Fine et al. (2018a, 2018b) of 50% is reasonable when making future plans for the maximum wave height, as we did not study here the full range of potential slip distributions of the Alaska subduction zone, and found occasional discrepancies. Therefore, where our numerical experiment shows a maximum 1.1 m tsunami at Prince Rupert, predicted at Seal Cove, a maximum realistic tsunami safe height of 1.65 m over MHHW should be considered, with the inclusion of a 50% safety factor (or 3.95 m above to MSL). This maximum safe height is the same after the addition of 1 m sea level rise to represent the effect of climate change in the region, which corresponds to a safe height of about 2.65 m above current MHHW (or 4.95 m above current MSL). The maximum wave induced velocity is about 3.0 m/s west of BC Terminal and in Fern Passage, with local maxima up to 4.0 m/s. At Seal Cove, the wave induced velocities are up to 0.15 m/s.

ACKNOWLEDGEMENTS

We would like to thank Dr. Tania Lado Insua for her assistance in starting these simulations and providing copies of the initial tsunami sources. We also would like to thank Dr. Lucinda Leonard for her helpful reviews and precious help on identification of the co-seismic hazards in the region of Haida Gwaii.

REFERENCES

Abadie, S., Harris, J.C., Grilli, S.T, Fabre R. 2012. Numerical modeling of tsunami waves generated by the flank collapse of the Cumbre Vieja Volcano (La Palma, Canary Islands): tsunami source and near field effects. *J. Geophys. Res.*, 117, C05030, doi:10.1029/2011JC007646.

Anderson, P. S., Gow, G. A. 2004. An assessment of the B. C. tsunami warning system and related risk reduction practices: tsunamis and coastal communities in British Columbia. 87 pp.

Atwatar, B.F., Nelson, A.R., Clague, J.J., Carver, G.A., Yamaguchi, D.K., Bobrowsky, P.T., Bourgeois, J., Darienzo, M.E., Grant, W.C., Hemphill-Haley, E., Kelsey, H.M., Jacoby, G.C., Nishenko, S.P., Palmer, S.P., Peterson, C.D., Reinhart M.A. 1995. Summary of Coastal Geologic Evidence for Past Great Earthquakes at the Cascadia Subduction Zone. Earthquake Spectra: Vol. 11, No. 1, pp. 1-18, doi:org/10.1193/1.1585800.

Bustin, A.M.M. 2006. The crustal structure, deformation from GPS, and seismicity related to oblique convergence along the Queen Charlotte margin, British Columbia. Ph.D. thesis, University of Victoria, Victoria, BC, Canada, 238p.

Cassidy, J.F., Rogers, G.C., Hyndman, R.D. 2014. An overview of the October 28, 2012 Mw 7.7 earthquake in Haida Gwaii, Canada: a tsunamigenic thrust event along a predominantly strike-slip margin, Pure Appl. Geophys., 171, doi:10.1007/s00024-014-0775-1.

Cassidy, J.F., Rogers, G.C., Lamontagne, M., Halchuk, S., Adams, J. 2010. Canada's Earthquakes: 'The Good, the Bad, and the Ugly', Geoscience Canada, 37 (1), 1–16.

Christensen, D. H., Beck, S. L. 1994. The rupture processes and tectonic implications of the great 1964 Prince William Sound earthquake. *Pure Applied Geophysics*. 142: 29-53.

Dunbar, D. S., LeBlond, P. H., Hodgins, D. O. 1988. Evaluation of tsunami levels along the British Columbia Coast. Seaconsult Marine Research Ltd. 208 pp.

Dunbar, P.K., Weaver, C.S. 2008. U.S. states and territories national tsunami hazard assessment - Historical record and sources for waves: Technical Report, National Oceanic and Atmospheric Administration and U.S. Geological Survey, 59 pp.

Fine, I.V., Cherniawsky J.Y, Thomson, R.E, Rabinovich A.B., Krassovski, M. V. 2015. Observations and numerical modelling of the 2012 Haida Gwaii Tsunami off the coast of British Columbia. Pure Appl. Geophys. v. 172, p. 699-718, doi 10.1007/s00024-014-1012-7

Fine, I. V., Thomson, R. E., Lupton, L. M., Mundschutz, S. 2018a. Numerical modelling of an Alaska 1964-type Tsunami at the Canadian Coast Guard Base in Seal Cove, Prince Rupert, British Columbia. Tech. Rep. Hydrogr. Ocean Sci. 321: v+ 33p.

Fine, I. V., Thomson, R. E., Lupton, L. M., Mundschutz, S. 2018b. Numerical modelling of a Cascadia subduction zone tsunami at the Canadian Coast Guard base in Seal Cove, Prince Rupert, British Columbia. Tech. Rep. Hydrogr. Ocean Sci. 322: v+ 34p.

Gao, D., Wang, K., Insua, T. L., Sypus, M., Riedel, M., Sun, T. 2018. Defining megathrust tsunami source scenarios for northernmost Cascadia. *Natural Hazards*. 94: 445-469. doi:10.1007/s11069-018-3397-6.

Geist, L. G., Parsons, T. 2006. Probabilistic analysis of tsunami hazards. *Natural Hazards*. 37: 277-314. doi:10.1007/s11069-005-4646-z

Goldfinger, C., Nelson, C. H., Morey, A. E., Johnson, J. E., Patton, J. R., Karabanov, E., Gutierrez-Pastor, J., Eriksson, A. T., Gracia, E., Dunhill, G., Enkin, R. J. 2012. Turbidite event history: Methods and implications for Holocene paleoseismicity of the Cascadia subduction zone. U.S. Geological Survey Professional Paper, 1661, 170.

Grilli, S.T., J.C. Harris, T. Tajalli-Bakhsh, T.L. Masterlark, C. Kyriakopoulos, J.T. Kirby and F. Shi 2013. Numerical simulation of the 2011 Tohoku tsunami based on a new transient FEM co-seismic source: Comparison to far- and near-field observations. *Pure and Applied Geophysics*, 170, 1333-1359, doi:10.1007/s00024-012-0528-y

Grilli S.T., O'Reilly C., Harris J.C., Tajalli-Bakhsh T., Tehranirad B., Banihashemi S., Kirby J.T., Baxter C.D.P., Eggeling T., Ma G. and F. Shi 2015. Modeling of SMF tsunami hazard along the upper US East Coast: Detailed impact around Ocean City, MD. *Natural Hazards*, 76(2), 705-746, doi: 10.1007/s11069-014-1522-8

Horrillo, J., Grilli, S. T., Nicolsky, D., Roeber, V., Zhang, J. 2014. Performance benchmarking tsunami operational models for NTHMP's inundation mapping activities. *Pure and Applied Geophysics*. 172: 869-884, doi: 10.1007/s00024-014-0891-y.

Hyndman, R.D. 2015. Tectonics and structure of the Queen Charlotte fault zone, Haida Gwaii, and large thrust earthquakes. Bull. Seismol. Soc. Am., 105(2B), 1058-1075, doi:10.1785/0120140181.

Ichinose, G., Somerville, P., Thio, H. K., Graves, R., O'Connell, D. 2007. Rupture process of the 1964 Prince William Sound, Alaska, earthquake from the combined inversion of seismic, tsunami, and geodetic data. *Journal of Geophysical Research*. 112, B07306, doi:1029/2006JB004728.

Johnson, J. M., Satake, K., Holdahl, S. R., Sauber, J. 1996. The 1964 Prince William Sound earthquake: Joint inversion of tsunami and geodetic data. *Journal of Geophysical Research*. 101(B1): 523-532.

Kirby, J. T., Shi, F., Tehranirad, B., Harris, J. C., Grilli, S. T. 2013. Dispersive tsunami waves in the ocean: Model equations and sensitivity to dispersion and Coriolis effects. *Ocean Modelling*. 62: 39-55. doi:10.1016/j.ocemod.2012.11.009.

Lane, E.M., Borrero, J., Whittaker, C.N., Bind, J., Chague-Goff, C., Goff, J., Goring, D., Hoyle, J., Mueller, C., Power, W.L., Reid, C.M., Williams, J.H., Williams, S.P. 2017. Effects of inundation by the 14th November, 2016 Kaikōura tsunami on Banks Peninsula, Canterbury, New Zealand. Pure Appl. Geophys. 174(5), 1855-1874, doi:10.1007/s00024-017-1534-x.

Leonard, L.J., Bednarski, J.M. 2014. Field survey following the 27 October 2012 Haida Gwaii tsunami, Pure Appl. Geophys., 171, doi:10.1007/s00024-014-0792-0.

Leonard, L.J., Rogers, G.C., Mazzotti, S. 2014. Tsunami hazard assessment of Canada. Natural Hazards, 70, 237-274, doi:10.1007/s11069-013-0809-5.

Leonard, L.J., Rogers, G.C., Mazzotti, S. 2012. A preliminary tsunami hazard assessment of the Canadian Coastline. Geological Survey of Canada, Open File 7201, 119 p, doi:10.4095/292067.

Liang, D., Borthwick, A. G., Romer-Lee, J. K. 2011. Run-up of solitary waves on twin conical islands using a Boussinesq model. *Journal of Offshore Mechanics and Arctic Engineering*. 134 (1): 011102-011102-9. doi:10.1115/1.4003394.

Li, L., Switzer, A. D., Wang, Y., Chan C., Qiu Q., Weiss, R. 2018. A modest 0.5-m rise in sea level will double the tsunami hazard in Macau. Science Advances. 4(8): eaat1180. doi: 10.1126/sciadv.aat118.

Ludwin, R.S., Dennis, R., Carver, D., McMillan, A.D., Losey, R., Clague, J., Jonientz-Trisler, C., Bowechop, J., Wray, J., and James, K., 2005. Dating the 1700 Cascadia earthquake: Great coastal earthquakes in Native stories: Seismological Research Letters, v. 76, no. 2, p. 140–148, doi: 10.1785/gssrl.76.2.140.

Madsen, P. A., Fuhrman, D. R., Schäffer, H. A. 2008. On the solitary wave paradigm for tsunamis. *Journal of Geophysical Research*. 113: C12012. doi:10.1029/2008JC004932

Nelson, A. R., Briggs, R. W., Dura, T., Engelhart, S. E., Gelfenbaum, G., Bradley, L-A., Forman, S. L., Vane, C. H., Kelley, K. A. 2015. Tsunami recurrence in the eastern Alaska-Aleutian arc: A Holocene stratigraphic record from Chirikof Island, Alaska. *Geosphere*. 11: 1172-1203. doi:10.1130/GES01108.1

Nykolaishen, L., Dragert, H., Wang, K., James, T.S., Schmidt, M. 2014. GPS observations of crustal deformation associated with the Mw 7.7 2012 Haida Gwaii earthquake. Bull. Seism. Soc. Amer. Vol. 105, No. 2B, pp. –, May 2015, doi: 10.1785/0120140177.

Nemati, F., Grilli, S.T., Ioualalen, M., Boschetti, L., Larroque, L. and J. Trevisan 2018. High-resolution coastal hazard assessment along the French Riviera from co-seismic tsunamis generated in the Ligurian fault system. *Natural Hazards*, pp. 1-34, doi.org/10.1007/s11069-018-3555-x

Ristau, J., Rogers, G.C., Cassidy, J.F. 2007. Stress in western Canada from regional moment tensor analysis, Canadian Journal of Earth Sciences, v. 44, p. 127-148, doi:10.1139/E06-057.

Shelby, M., Grilli, S. T. and Grilli, A. R., 2016. Tsunami hazard assessment in the Hudson River Estuary based on dynamic tsunami-tide simulations. *Pure and Applied Geophysics*, 173(12), 3,999-4,037, doi:10.1007/s00024-016-1315-y

Shi, F., Kirby, J. T., Harris, J. C., Geiman, J. D., Grilli, S. T. 2012. A high-order adaptive time-stepping TVD solver for Boussinesq modeling of breaking waves and coastal inundation. *Ocean Modelling*. 43-44: 36:51. doi:10.1016/j.ocemod.2011.12.004.

Stefanakis, T. S., Contal, E., Vyatis, N., Dias, F., Synolakis, C. E. 2014. Can small islands protect nearby coasts from tsunamis? An active experimental design approach. Proceedings of the Royal Society A: Mathematical, Physical and Engineering Sciences. 470: 20140575.

Suito, H., Freymueller, J. T. 2009. A viscoelastic and afterslip postseismic deformation model for the 1964 Alaska earthquake. *Journal of Geophysical Research*. 114, B11404, doi:10.1029/2008JB005954.

Wigen, S. O., White, W. R. H. 1964. Tsunami of March 27-29, 1964: West coast of Canada. Canada Department of Mines and Technical Surveys. 13 pp.

Wronna, M., Omira, R., Baptista, M. A. 2015. Deterministic approach for multiple-source tsunami hazard assessment for Sines, Portugal. *Natural Hazards and Earth System Sciences*. 15: 2557-2568, doi: 10.5194/nhess-15-2557-2015.

ANNEXE A: WAVE PROPAGATION IN THE ALASKA CASE

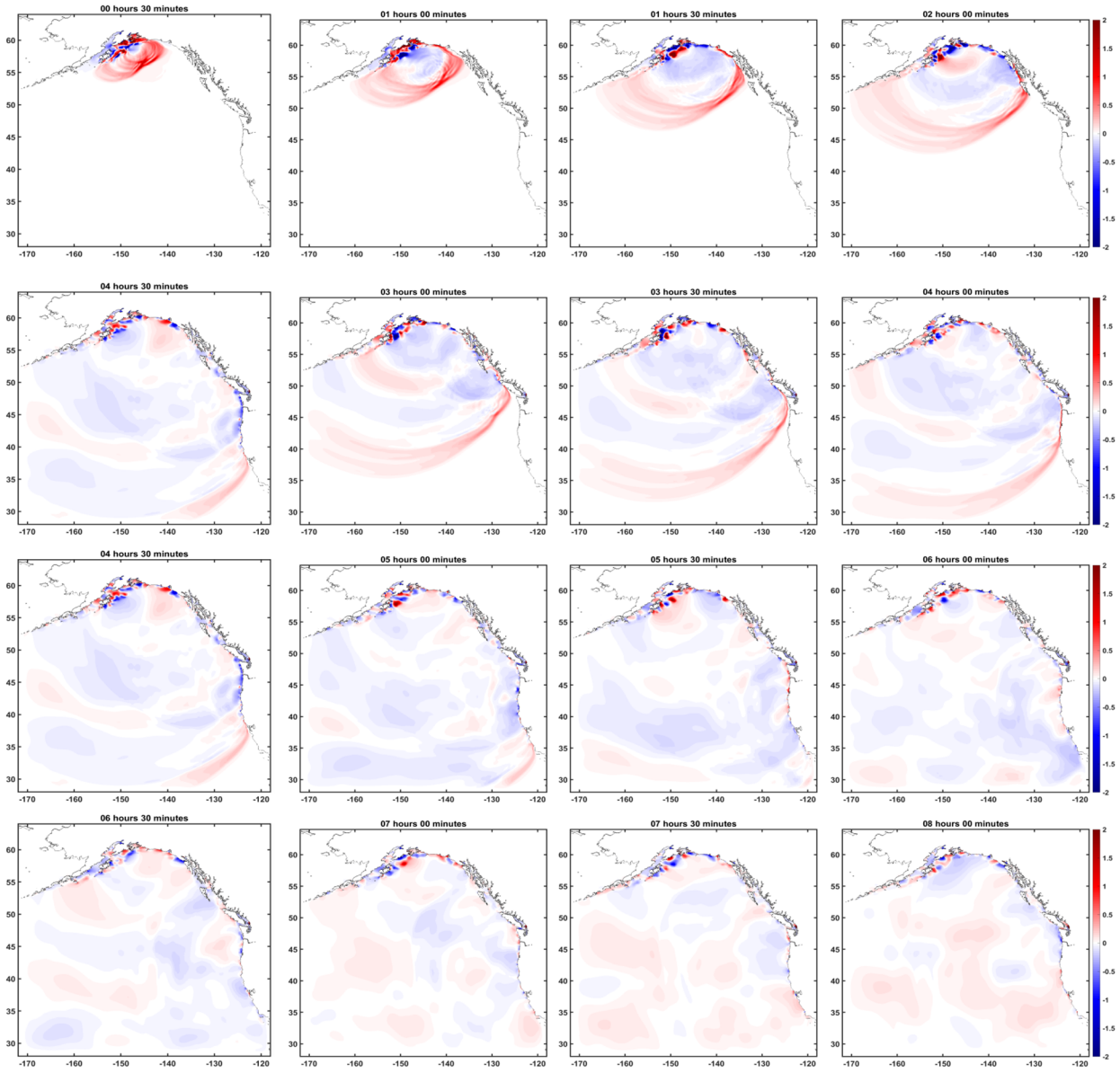

Figure A1: Wave amplitude in G0. Each frame are a snapshot of the amplitude with 30 minutes increment, from 0h30 to 8h00 after the earthquake.

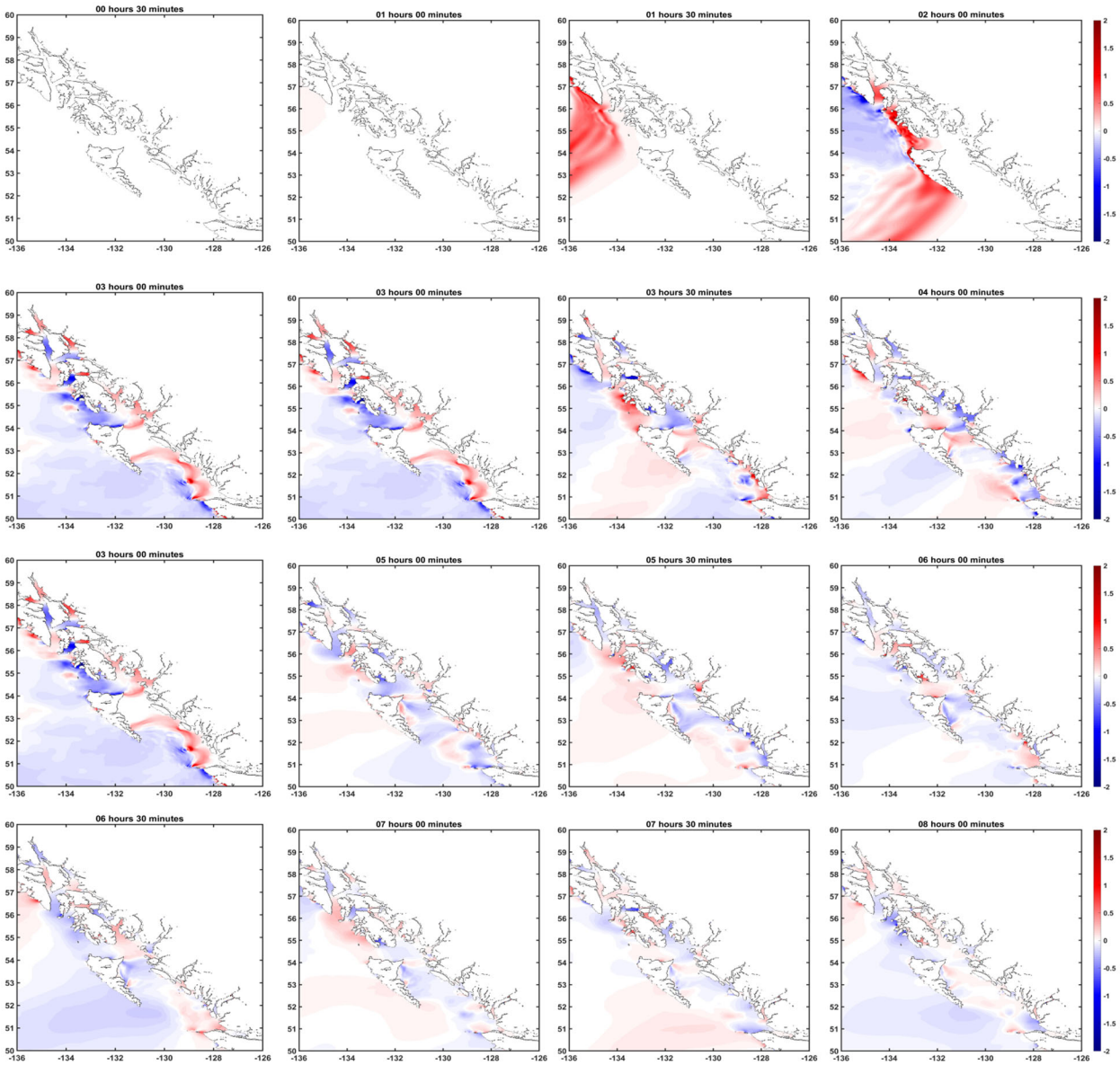

Figure A2: Wave amplitude in G1. Each frame are a snapshot of the amplitude with 30 minutes increment, from 0h30 to 8h00 after the earthquake.

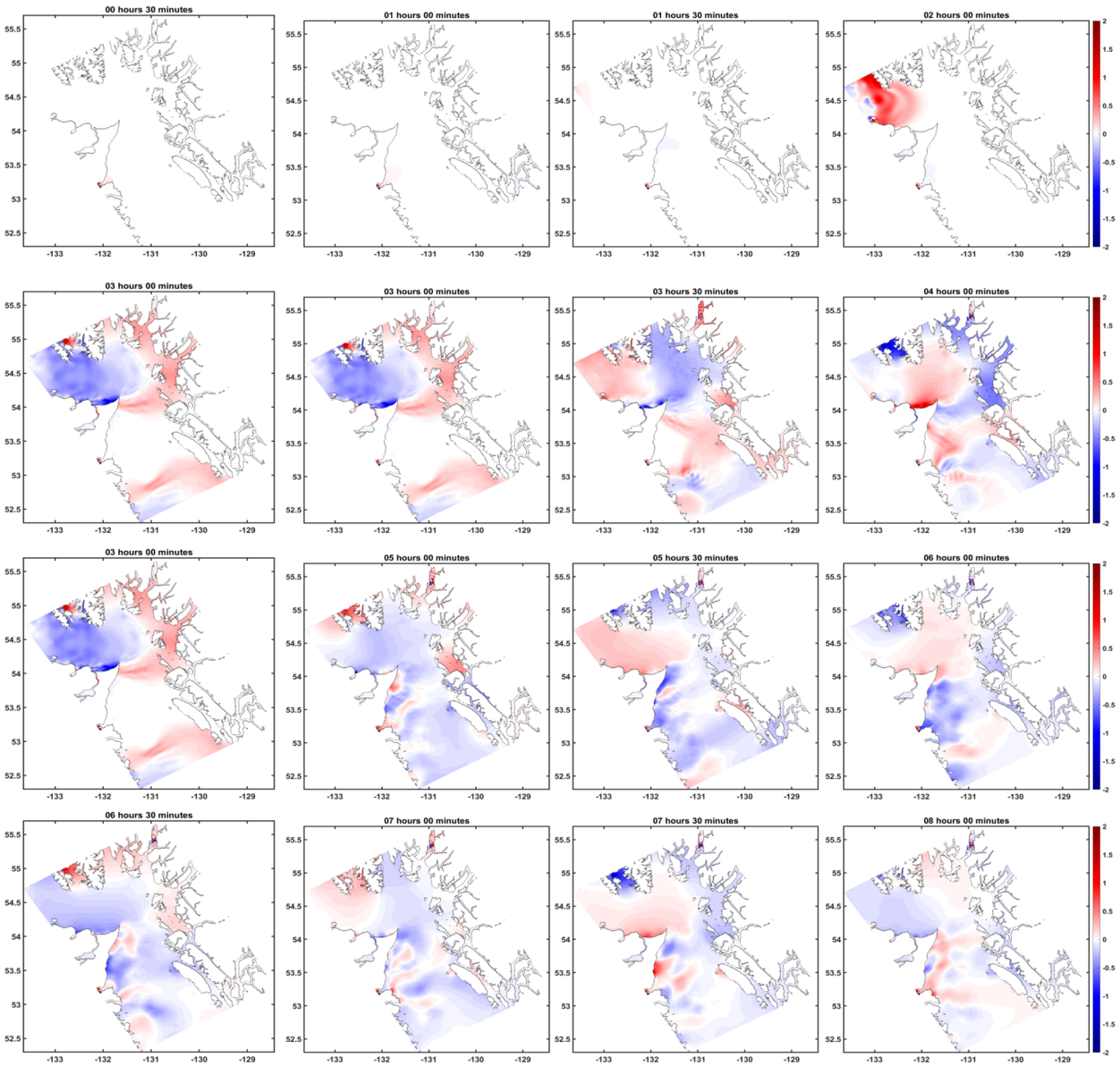

Figure A3: Wave amplitude in G2. Each frame is a snapshot of the amplitude with 30 minutes increment, from 0h30 to 8h00 after the earthquake.

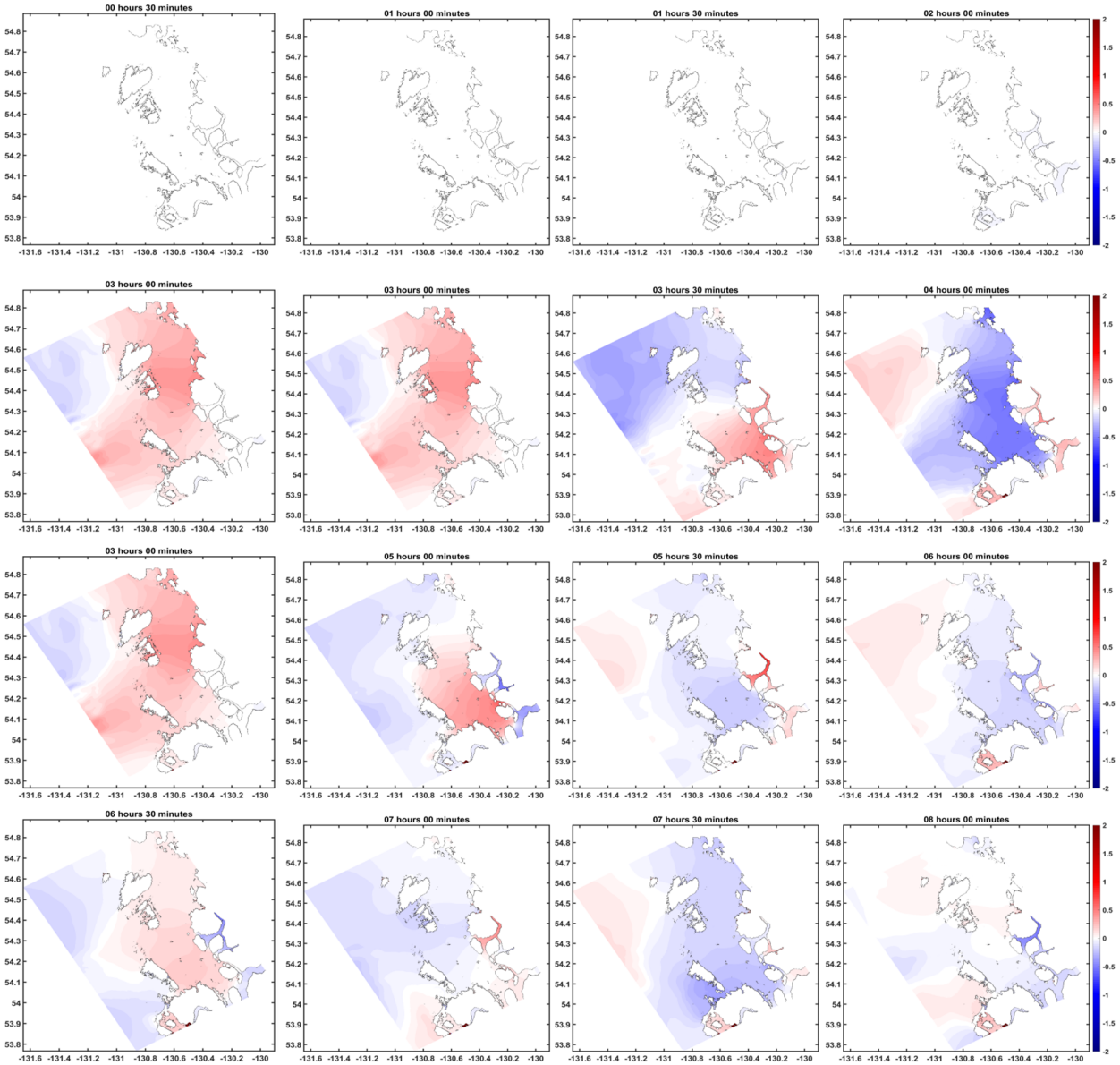

Figure A4: Wave amplitude in G3. Each frame is a snapshot of the amplitude with 30 minutes increment, from 0h30 to 8h00 after the earthquake.

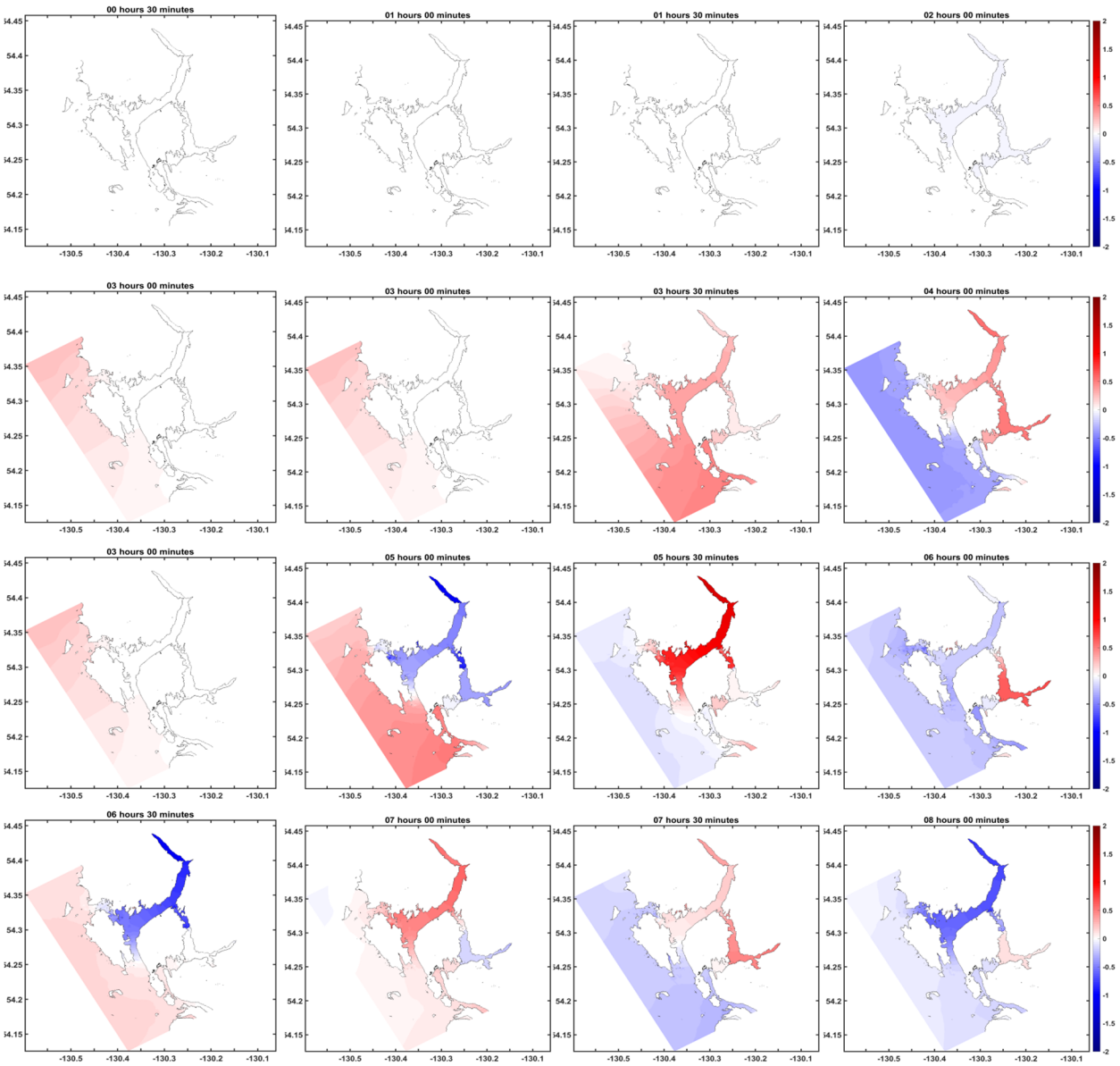

Figure A5: Wave amplitude in G4. Each frame is a snapshot of the amplitude with 30 minutes increment, from 0h30 to 8h00 after the earthquake.

ANNEXE B: WAVE PROPAGATION IN THE CASCADIA CASE

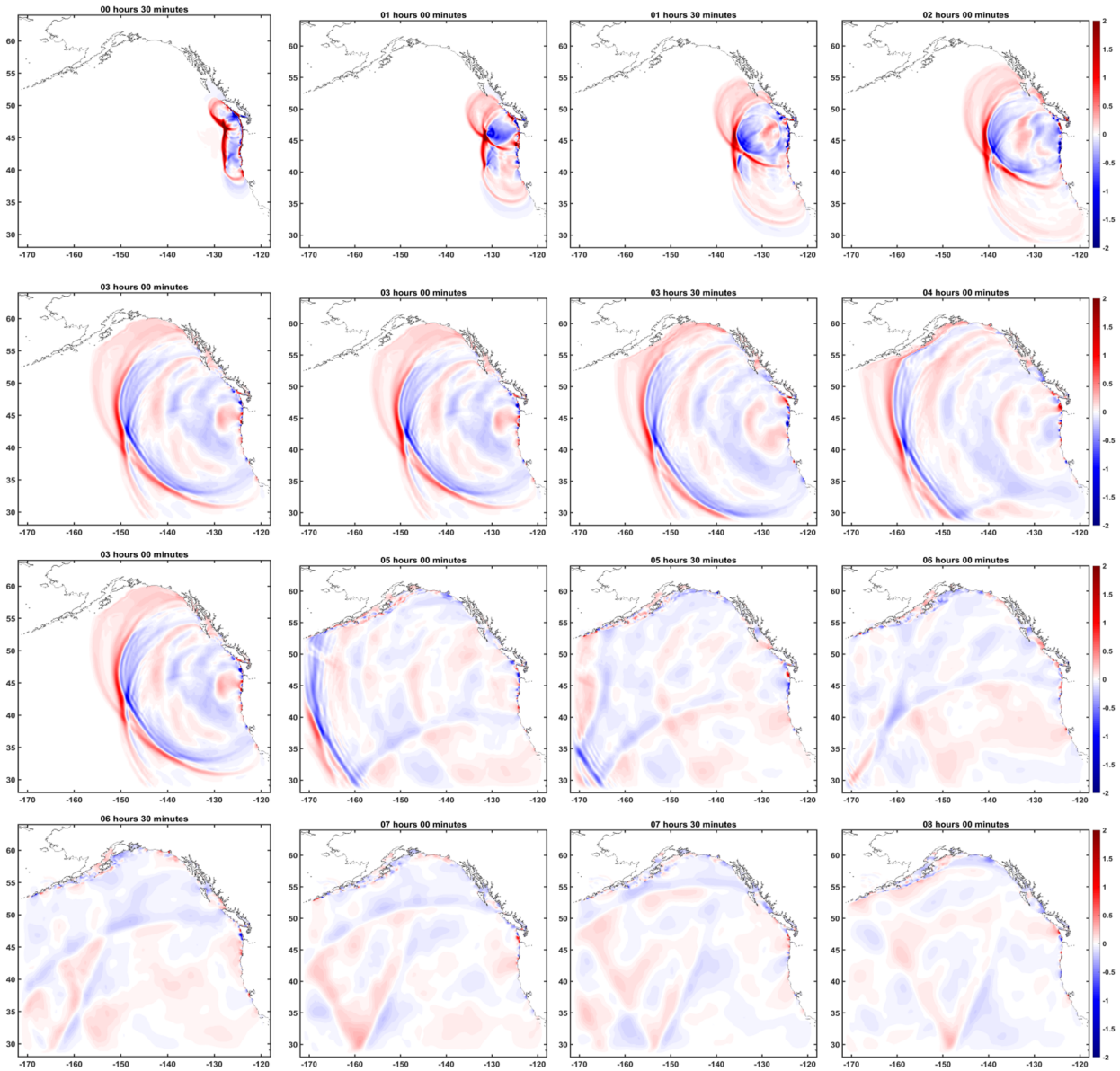

Figure B1: Wave amplitude in G0. Each frame is a snapshot of the amplitude with 30 minutes increment, from 0h30 to 8h00 after the earthquake.

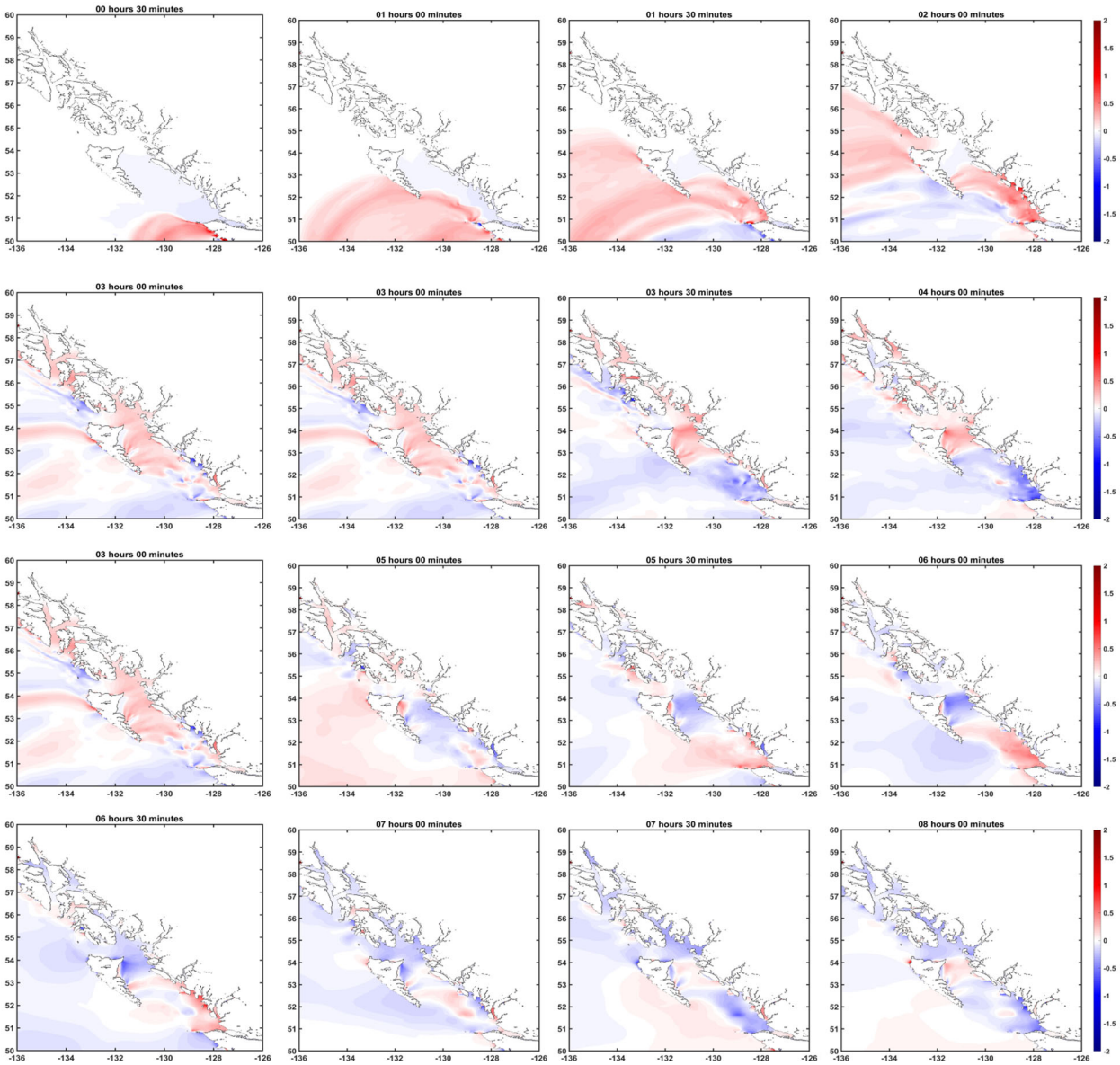

Figure B2: Wave amplitude in G1. Each frame is a snapshot of the amplitude with 30 minutes increment, from 0h30 to 8h00 after the earthquake.

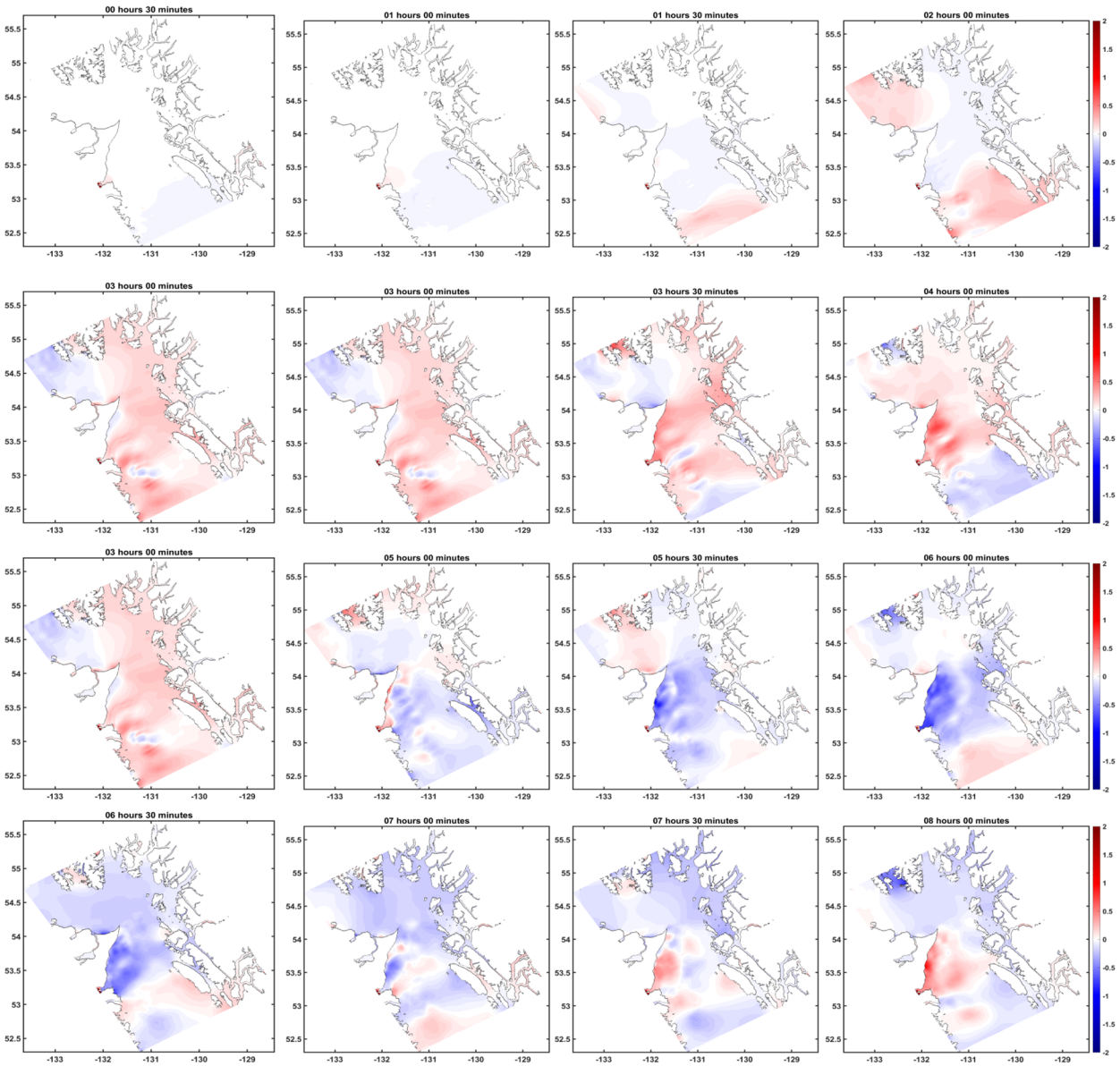

Figure B3: Wave amplitude in G2. Each frame is a snapshot of the amplitude with 30 minutes increment, from 0h30 to 8h00 after the earthquake.

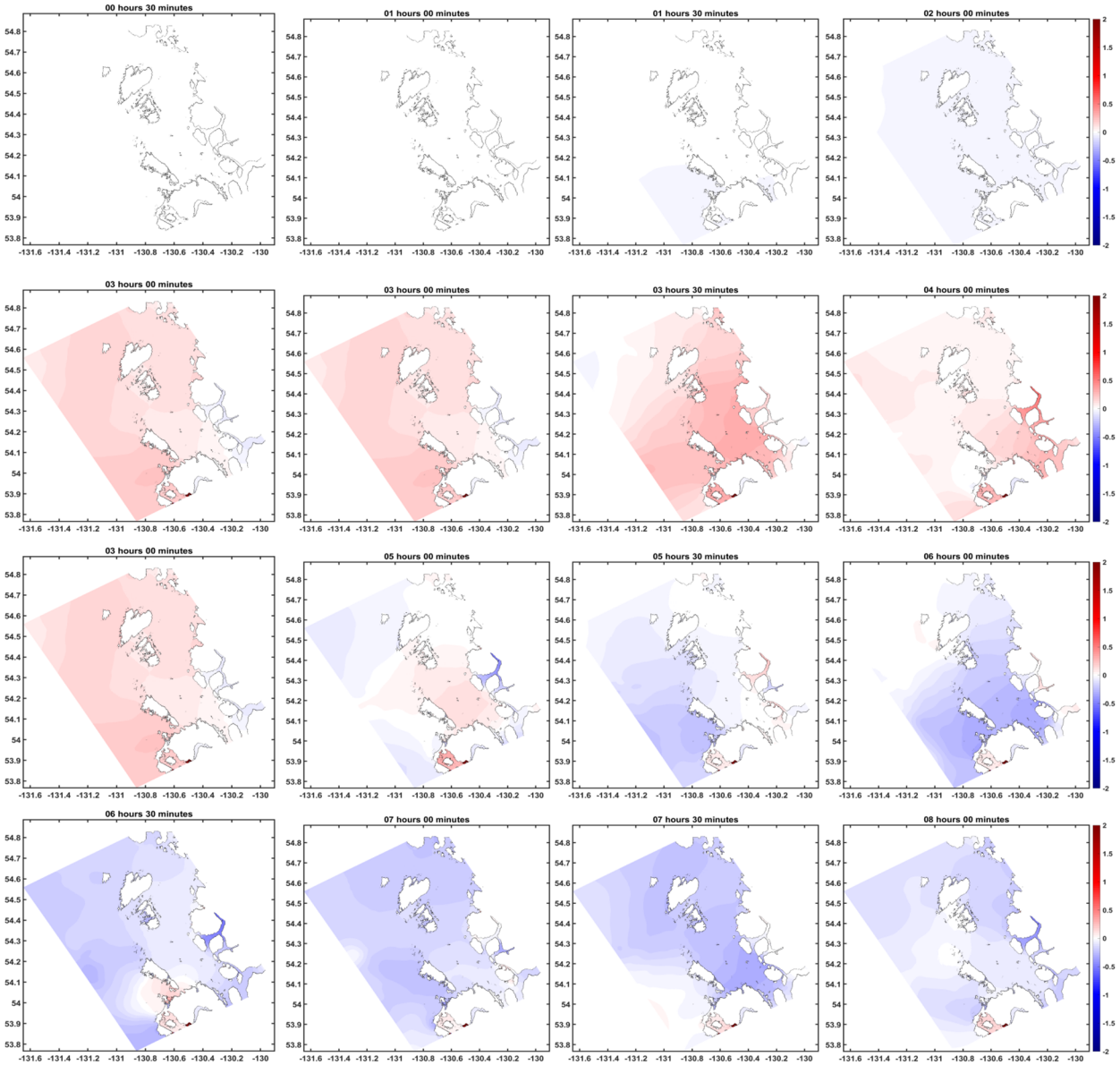

Figure B4: Wave amplitude in G3. Each frame is a snapshot of the amplitude with 30 minutes increment, from 0h30 to 8h00 after the earthquake.

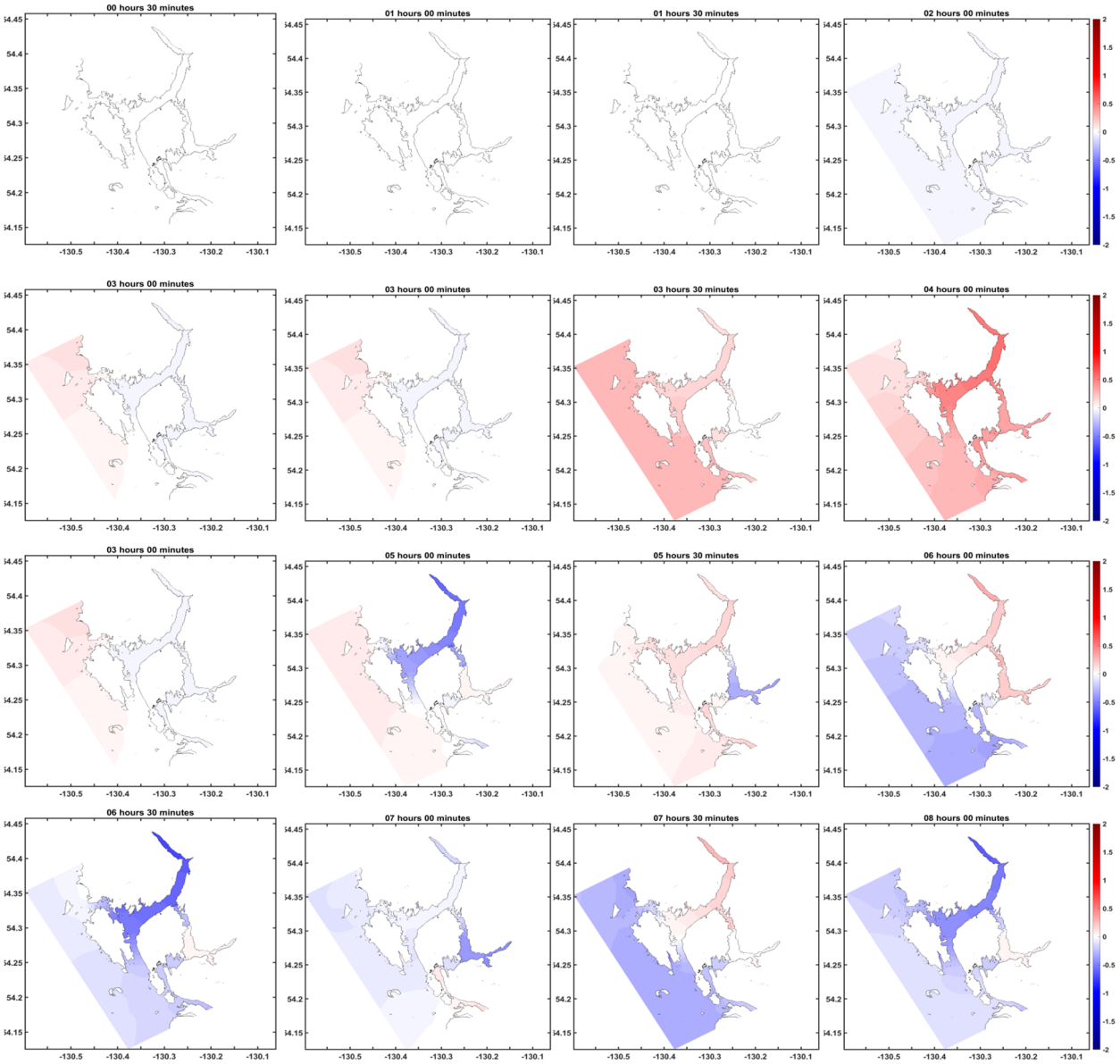

Figure B5: Wave amplitude in G4. Each frame is a snapshot of the amplitude with 30 minutes increment, from 0h30 to 8h00 after the earthquake.

ANNEXE C: MAP OF THE REGION OF PRINCE RUPERT

Figure C1: Map of the region of Prince Rupert. Key locations have been highlighted. Original figure from Google Earth.